Deliverable 4.3:

Final Results on Adaptive Directional LOS and NLOS Reliable Connectivity

Editor:	Marco Di Renzo, CNRS	
Deliverable nature:	Document, report (R)	
Dissemination level:	Public (PU)	
Date: planned | actual	30 April 2022	30 April 2022
Version | No. of pages	1.0	69
Keywords:	Reconfigurable intelligent surfaces, D-band	

Abstract

Deliverable D4.3 reinforces and generalizes the results of the research activities conducted and summarised in deliverable D4.1 on ``Initial results on adaptive directional LOS and NLOS reliable connectivity''. In this direction, the present deliverable focuses on optimization and machine learning techniques tailored to the physical and medium access layers requirements of fully reconfigurable environments. Overall, the results reported in this deliverable allowed us to assess the major performance gains that the deployment of RISs in high frequency bands bring about for application to future wireless communication systems.

This project has received funding from the European Union's Horizon 2020 research and innovation programme under grant agreement No 871464. This publication reflects only the author's view and the European Commission is not responsible for any use that may be made of the information it contains.

Impressum

Full project title: Artificial Intelligence Aided D-band Network for 5G Long Term Evolution

Short project title: ARIADNE

Number and title of work-package: WP4 - D-Band wireless network optimization leveraging ML principles

Number and title of task: Task 4.1 – Adaptive Directional LOS and NLOS reliable connectivity

Document title: Final Results on Adaptive Directional LOS and NLOS Reliable Connectivity

assessment, and algorithm designs

Editor: Marco Di Renzo, CNRS

Work-package leader: CNRS

Copyright notice

List of Authors

Company	Authors	Contribution
CNRS	Marco Di Renzo	Editor and contribution to Chapter 1 and Chapter 3
CNRS	Nour Awarkeh	Editor and contribution to Chapter 1 and Chapter 3
CNRS	Xuewen Qian	Editor and contribution to Chapter 1 and Chapter 3
UOULU	Jiguang He	Contributions to Chapter 1
UOULU	Markku Juntti	Contributions to Chapter 1
UOULU	Joonas Kokkoniemi	Review of the document
NCSRD	Fotis Lazarakis Dimitrios Selimis Kyriakos Manganaris	Contribution to Chapters 2 and 4
EURESCOM	Halid Hrasnica	Final review
UPRC	Angeliki Alexiou	Final review
RapidMiner	Rachana Desai	Contribution to Chapter 5
RapidMiner	Edwin Yaqub	Contribution to Chapter 5
UPRC	Giorgos Stratidakis	Contribution to Chapter 6
UPRC	Sotiris Droulias	Contribution to Chapter 6

Final Results on Adaptive Directional LOS and NLOS Reliable Connectivity

List of Figures

List of Tables

Executive Summary

Deliverable D4.3 reinforces and generalizes the results of the research activities conducted and summarised in deliverable D4.1 on “Initial results on adaptive directional LOS and NLOS reliable connectivity”. In this direction, the present deliverable focuses on optimization and machine learning techniques tailored to the physical and medium access layers requirements of fully reconfigurable environments.

More specifically, this deliverable consists of six chapters whose contribution is briefly summarized as follows.

In **Chapter 1**, we apply one special type of deep neural networks (DNNs) framework, known as model-driven deep unfolding neural network, to reconfigurable intelligent surface (RIS)-aided single-input multiple-output (SIMO) systems. We focus on uplink cascaded channel estimation, where known and fixed base station combining and RIS phase control matrices are considered for collecting observations. To boost the estimation performance and reduce the training overhead, the inherent channel sparsity of high frequency channels is leveraged in the deep unfolding method. It is verified that the proposed deep unfolding network architecture can outperform the least squares (LS) and atomic norm minimization (ANM) methods with a relatively smaller training overhead and online computational complexity.

In **Chapter 2**, we present a comprehensive reconfigurable intelligent surface (RIS) power consumption model that captures its main power-consuming electronic components and we propose an energy harvesting model used for extracting the RIS harvested power and for formulating the optimization problem of interest. In particular, we focus on the optimal RIS placement as well as the amplitude and phase response adjustment of the reflective units (RUs) for maximizing the end-to-end signal-to-noise ratio (SNR), subject to the harvested power being sufficient for RIS autonomous operation. In addition, an analytical solution is provided for the amplitude and phase response optimal values of the RUs. Through simulations, we provide a range of average power consumption of the RIS electronics that guarantees its autonomous operation.

In **Chapter 3**, we present four typical RIS-aided multi-user scenarios with special emphasis on medium access control (MAC) schemes. We then propose and elaborate upon centralized, distributed and hybrid artificial-intelligence (AI)-assisted MAC architectures in RIS-aided multi-user communications systems. Finally, we discuss some challenges, perspectives and potential applications of RISs as they are related to MAC design.

In **Chapter 4**, we describe the upgrade of a system level simulation model for D-band networks in realistic environments that was introduced in D4.2. In comparison with the initial aspect of the system simulation model, this version is enhanced in several directions. The main differences concern user's mobility model and path loss modelling. Particularly, the trajectories of the user have extra degrees of randomness and therefore, they have a greater diversity. Regarding the path loss modelling, in this refined version of the model a large scale fading term was added to the received power balance. This term forces user's received power to change into a stochastic quantity.

In **Chapter 5**, we analyze the challenges and opportunities for machine learning in the channel modeling domain for both line of sight (LOS) and non-line of sight (NLOS) scenarios in order to understand the feasibility of predicting LOS connectivity at the physical layer. We present analysis and results on the application of machine learning to predict LOS blockages, instead of just identifying them using computationally expensive blockage identification methods.

In **Chapter 6**, we study the relation between the received power and the position, orientation and size of RISs. In this context, we perform simulations to understand the RIS efficiency under both full and partial illumination.

Overall, the results reported in this deliverable allowed us to assess the major performance gains that the deployment of RISs in high frequency bands bring about for application to future wireless communication systems.

Chapter 1

Deep Unfolding for Estimating RIS-Aided Channels

1.1 Introduction

Reconfigurable intelligent surfaces (RISs) have recently been introduced for enhanced energy efficiency (EE), spectrum efficiency (SE), positioning accuracy, as well as network/physical-layer security [1–5]. The RIS, either being passive, active, or a hybrid combination of the former two, is used to smartly control the radio propagation environment, by virtue of multi-function capabilities, e.g., reflection, refraction, diffraction, scattering, and even absorption [6]. In the literature, the RIS is commonly used as an intelligent reflector, which breaks the well-known law of reflection [7], to mitigate the blockage effect and expand the connectivity range, especially for millimeter wave (mmWave) communications and terahertz (THz). However, the RIS is commonly assumed to be nearly-passive. That is, no power amplifiers and baseband processing units are available at the RIS. Besides, in order to compensate for the additional path loss in the reflection route via the RIS, a large number of RIS elements must be employed. These make the channel state information (CSI) acquisition difficult to tackle in practice. Note that the channel estimation (CE) can only be performed either at the base station (BS) or at the mobile station (MS).

Since the RIS phase control and joint active and passive beamforming are sensitive to the CSI accuracy, the full potential of RIS cannot be achieved when the CE is poorly performed. Therefore, accurate yet efficient CE methods for the individual channels or the cascaded channel are of vital importance. In our previous works, we took advantage of the inherent channel sparsity and rank-deficiency features of high frequency multiple-input multiple-output (MIMO) channels and we applied the iterative reweighted method and the atomic norm minimization (ANM) method for estimating the channel parameters of RIS-aided MIMO systems [8, 9]. In another recent work [10], sparse matrix factorization and matrix completion were exploited in a sequential manner to facilitate the CE process. These works fall into the category of conventional model-based approaches, which suit only for a small- or medium-sized RIS, BS, and MS.

As the number of RIS elements and BS/MS antennas continues to grow (this is an inevitable trend at high frequencies), more training overhead to obtain adequate CE performance, within the channel coherence time, via conventional model-based methods is required. Besides, the associated computational complexity will become inevitably high. These considerations motivate the application of data-driven or hybrid approaches for CE in RIS-aided communications [11,12]. In [13], a convolutional neural network (CNN) was considered for RIS CE in a multi-user scenario. Therein, however, each user needs to first estimate its own channel and then map the estimate to the corresponding ground-truth channel, which naturally increases the computational complexity. Therefore, in this study, we resort to a model-driven deep unfolding approach, which has already been used in MIMO detection and sparse signal recovery [14, 15], for estimating the cascaded channel in RIS-aided mmWave single-input multiple-output (SIMO) systems [16]. To the best of the authors' knowledge, the concept of deep unfolding has not yet been considered for RIS CE. Also, unlike the fully-connected neural network with received pilot signal being the input and cascaded channel being the output, deep unfolding is capable of learning and capturing the dynamics of the time-varying wireless channels.

Deep unfolding mimics the operation of conventional (projected) gradient descent algorithms, and it is capable of directly mapping the received pilot signals to the cascaded channel. Its computationally intensive training process can be executed offline and the online implementation/prediction phase only entails low-complexity calculations, e.g., matrix multiplications and additions, and element-wise operations. Besides, the step sizes and regularization parameters can be combined and optimized during the training of the deep unfolding model, which is not possible in traditional gradient descent methods. In this study, specifically, the rank-deficiency property of the cascaded channel is explicitly considered in the deep unfolding framework. It is verified that the deep unfolding scheme can outperform the least squares (LS) estimation and the ANM methods [9] in terms of normalized mean square error (NMSE) with a smaller training overhead and a reduced online computational complexity.

Notations: A bold lowercase letter $\mathbf{a}$ denotes a vector, and a bold capital letter $\mathbf{A}$ denotes a matrix. $(\cdot)^{\mathsf{T}}$ and $(\cdot)^{\mathsf{H}}$ denote the matrix or vector transpose and Hermitian transpose, respectively. $\mathrm{diag}(\mathbf{a})$ denotes a square diagonal matrix with the entries of $\mathbf{a}$ on its diagonal, $\mathbb{E}[\cdot]$ is the expectation operator, $\mathbf{0}$ denotes the all-zero vector, $\mathbf{I}_M$ denotes the $M \times M$ identity matrix, and $j = \sqrt{-1}$. $\|\cdot\|_{\mathrm{F}}$ and $\|\cdot\|_*$ denote the Frobenius norm and nuclear norm of a matrix, respectively, and $\|\cdot\|_2$ denotes the Euclidean norm of a vector.

1.2 System Model

We consider a nearly-passive RIS-aided SIMO network, where the MS communicates with the BS via the RIS, as shown in Fig. 1.1. The BS and RIS are equipped with multiple antennas and with nearly-passive scattering elements, respectively, while the MS is equipped with a single antenna. We further assume that the direct MS-BS channel is blocked.[1] The RIS-BS channel, which is denoted as $\mathbf{H}_1 \in \mathbb{C}^{M \times N}$ with M and N being the number of antennas and scattering elements at the BS and RIS, respectively,

---

[1] When the direct MS-BS channel exists, we can estimate it by setting the RIS into an absorption mode. Then, we can estimate the cascaded channel by subtracting the direct MS-BS channel. Such a two-stage procedure is sufficient for estimating all the channel components between the BS and MS. However, in this work, we only focus on the cascaded channel estimation, appearing at the second stage.

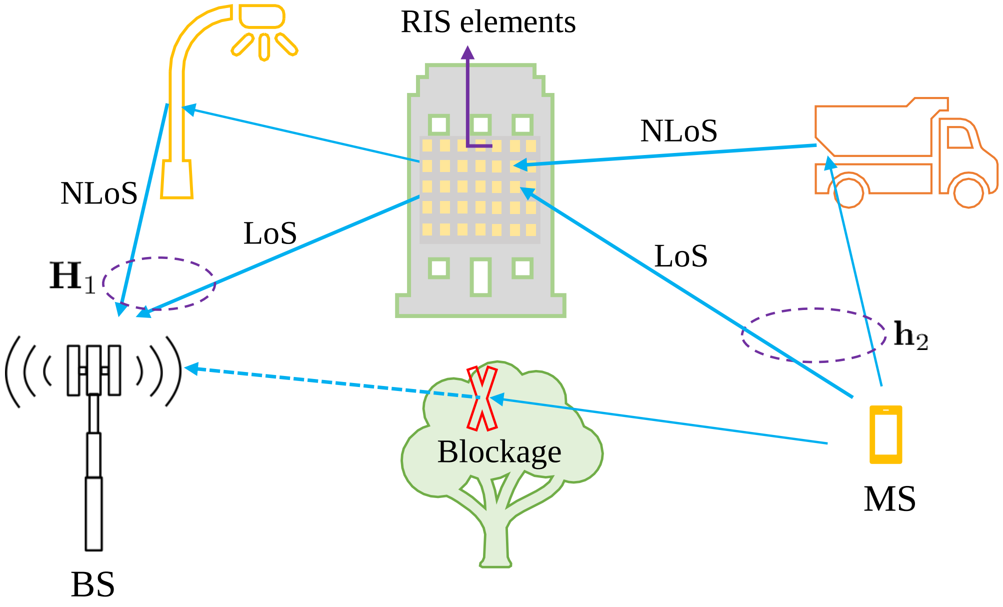

Figure 1.1: A typical scenario for maintaining the connectivity by deploying an RIS in a SIMO network.

can be written as

$$\mathbf{H}_1 = \sum_{i=1}^{L_1} g_{1,i}\boldsymbol{\alpha}(\phi_{1,i})\boldsymbol{\alpha}^{\mathsf{H}}(\theta_{1,i}) = \mathbf{A}(\boldsymbol{\phi}_1)\mathrm{diag}(\mathbf{g}_1)\mathbf{A}^{\mathsf{H}}(\boldsymbol{\theta}_1), \tag{1.1}$$

where $L_1 \ll \min\{M, N\}$ is the number of channel paths, including one line-of-sight (LoS) path (with $i = 1$) and multiple non-line-of-sight (NLoS) paths (with $i > 1$), and $g_{1,i} \in \mathbb{C}$, $\theta_{1,i} \in \mathbb{R}$, and $\phi_{1,i} \in \mathbb{R}$ denote the propagation path gain, the angle of departure (AoD), and the angle of arrival (AoA) associated with the ith propagation path. The array response vector $\boldsymbol{\alpha}(\phi_{1,i}) \triangleq [1, \quad e^{j\pi\sin(\phi_{1,i})}, \ldots, e^{j(M-1)\pi\sin(\phi_{1,i})}]^{\mathsf{T}} \in \mathbb{C}^{M\times 1}$ is obtained by assuming half-wavelength inter-element spacing, and $\boldsymbol{\alpha}(\theta_{1,i}) \in \mathbb{C}^{N\times 1}$ can be formulated in the same manner. We assume $g_{1,1} \sim \mathcal{CN}(0, \sigma^2_{\mathsf{LoS}})$, and define the vectors $\tilde{\mathbf{g}}_1 \triangleq [g_{1,2}, \ldots, g_{1,L_1}]^{\mathsf{T}} \sim \mathcal{CN}(\mathbf{0}, \sigma^2_{\mathsf{NLoS}}\mathbf{I}_{L_1-1})$, $\mathbf{g}_1 \triangleq [g_{1,1}, \tilde{\mathbf{g}}_1^{\mathsf{T}}]^{\mathsf{T}}$, $\boldsymbol{\phi}_1 \triangleq [\phi_{1,1}, \ldots, \phi_{1,L_1}]^{\mathsf{T}}$, $\boldsymbol{\theta}_1 \triangleq [\theta_{1,1}, \ldots, \theta_{1,L_1}]^{\mathsf{T}}$, $\mathbf{A}(\boldsymbol{\phi}_1) \triangleq [\boldsymbol{\alpha}(\phi_{1,1}), \ldots, \boldsymbol{\alpha}(\phi_{1,L_1})]$, and $\mathbf{A}(\boldsymbol{\theta}_1) \triangleq [\boldsymbol{\alpha}(\theta_{1,1}), \ldots, \boldsymbol{\alpha}(\theta_{1,L_1})]$.

Similarly, the MS-RIS channel $\mathbf{h}_2 \in \mathbb{C}^{N\times 1}$ can be written as

$$\mathbf{h}_2 = \sum_{i=1}^{L_2} g_{2,i}\boldsymbol{\alpha}(\phi_{2,i}) = \mathbf{A}(\boldsymbol{\phi}_2)\mathbf{g}_2. \tag{1.2}$$

All the channel parameters in $\mathbf{h}_2$ are defined as those in $\mathbf{H}_1$. We also assume $g_{2,1} \sim \mathcal{CN}(0, \sigma^2_{\mathsf{LoS}})$, $\tilde{\mathbf{g}}_2 \triangleq [g_{2,2}, \ldots, g_{2,L_2}]^{\mathsf{T}} \sim \mathcal{CN}(\mathbf{0}, \sigma^2_{\mathsf{NLoS}}\mathbf{I}_{L_2-1})$, and define $\mathbf{g}_2 \triangleq [g_{2,1}, \tilde{\mathbf{g}}_2^{\mathsf{T}}]^{\mathsf{T}}$ and $\mathbf{A}(\boldsymbol{\phi}_2) \triangleq [\boldsymbol{\alpha}(\phi_{2,1}), \ldots, \boldsymbol{\alpha}(\phi_{2,L_2})]$ with $L_2 \ll N$.

The end-to-end uplink MS-RIS-BS channel (including the effect of the RIS) can be written as

$$\mathbf{h} = \mathbf{H}_1\boldsymbol{\Omega}\mathbf{h}_2 = \mathbf{H}_1\mathrm{diag}(\mathbf{h}_2)\boldsymbol{\omega}, \tag{1.3}$$

where $\boldsymbol{\Omega} = \mathrm{diag}(\boldsymbol{\omega})$ is the RIS phase control matrix, with $\boldsymbol{\omega} = [\omega_1, \ldots, \omega_N]^{\mathsf{T}}$ and $|\omega_i| = 1$ for $\forall i$ [1]. We are interested in low-cost and low-complexity implementations of RISs, we hence focus on RISs that can control only the phase response. It is worth noting that an RIS may be composed of an array of amplifiers with increased power consumption and hardware complexity [17]. In this case, the unit-modulus constraint on each element ω_i can be relaxed.

In (1.3), $\mathbf{H}_1\mathrm{diag}(\mathbf{h}_2)$ is referred to as the cascaded channel. By knowing it, we can optimize the RIS phase control matrix and BS beamforming/combining vector. Let us define it as $\mathbf{H}_c \in \mathbb{C}^{M\times N}$, i.e.,

$$\mathbf{H}_c = \mathbf{H}_1\mathrm{diag}(\mathbf{h}_2). \tag{1.4}$$

Based on the considered assumptions, we have $\mathrm{rank}(\mathbf{H}_1) = L_1$ and $\mathrm{rank}(\mathrm{diag}(\mathbf{h}_2)) = N$. Thus $\mathrm{rank}(\mathbf{H}_c) \leq \min\{\mathrm{rank}(\mathbf{H}_1), \mathrm{rank}(\mathrm{diag}(\mathbf{h}_2))\} = L_1$. The inherent channel sparsity (represented by the rank deficiency of the cascaded channel) can be applied in order to enable an efficient yet accurate CE of (1.4).

1.3 Learning to Estimate

In this section, we first introduce the channel sounding procedure, and then describe the optimization problem formulation for recovering the cascaded channel by using conventional (model-based) methods. Finally, we describe the model-driven deep unfolding method for estimating the rank-deficient cascaded channel.

1.3.1 Channel Sounding

During the sounding process, pilot signals are sent from the MS to the BS via the RIS. A different RIS phase control matrix is considered for each channel use while the combining matrix at the BS is fixed. The received signal at channel use k, for $k = 1, \ldots, K$, can be written as

$$\mathbf{y}[k] = \mathbf{W}^{\mathsf{H}}[k]\mathbf{H}_1\mathbf{\Omega}[k]\mathbf{h}_2 s[k] + \mathbf{W}^{\mathsf{H}}[k]\mathbf{n}[k], \tag{1.5}$$

where $\mathbf{W}[k] \in \mathbb{C}^{M\times N_{\mathsf{W}}}$ is the combining matrix at the BS with N_{W} denoting the number of columns,[2] $s[k]$ is the pilot signal sent by the MS, and $\mathbf{n}[k] \sim \mathcal{CN}(0, \sigma^2)$ is the additive white Gaussian noise (AWGN) at the BS.

The received signal $\mathbf{y}[k]$ in (1.5) can be reformulated as

$$\mathbf{y}[k] = \mathbf{W}^{\mathsf{H}}[k]\mathbf{H}_c\boldsymbol{\omega}[k]s[k] + \mathbf{W}^{\mathsf{H}}[k]\mathbf{n}[k], \tag{1.6}$$

where $\mathbf{\Omega}[k] = \mathrm{diag}(\boldsymbol{\omega}[k])$.

Without loss of generality, we assume $s[1] = s[K] = 1$ and $\mathbf{W}[1] = \mathbf{W}[K] = \mathbf{W}$. The received signals $\mathbf{Y} = [\mathbf{y}[1], \ldots, \mathbf{y}[K]]$ can be rewritten as

$$\mathbf{Y} = \mathbf{W}^{\mathsf{H}}\mathbf{H}_c\bar{\mathbf{\Omega}} + \mathbf{W}^{\mathsf{H}}\mathbf{N}, \tag{1.7}$$

where $\bar{\mathbf{\Omega}} = [\boldsymbol{\omega}[1], \ldots, \boldsymbol{\omega}[K]]$ and $\mathbf{N} = [\mathbf{n}[1], \ldots, \mathbf{n}[K]]$. An additional vectorization step is considered for all the terms in (1.7), resulting in

$$\mathbf{y} = (\bar{\mathbf{\Omega}}^{\mathsf{T}} \otimes \mathbf{W}^{\mathsf{H}})\mathbf{h}_c + \mathbf{n}, \tag{1.8}$$

---

[2] We consider an analog combining matrix, which is a suitable choice for fulfilling the requirements of reduced-complexity hybrid precoding architectures commonly assumed for MIMO transceivers. When $N_{\mathsf{W}} > N_{\mathsf{RF}}$, with N_{RF} being the number of radio frequency (RF) chains at the BS, we need $K\lceil N_{\mathsf{W}}/N_{\mathsf{RF}}\rceil$ channel uses to complete the sounding process. Otherwise, K channel uses are sufficient.

where $\mathbf{y} = \mathrm{vec}(\mathbf{Y}), \mathbf{h}_c = \mathrm{vec}(\mathbf{H}_c)$, and $\mathbf{n} = \mathrm{vec}(\mathbf{W}^{\mathsf{H}}\mathbf{N})$. Based on the vectorized received signal $\mathbf{y}$, we need to estimate the vectorized cascaded channel $\mathbf{h}_c$. Let us define $\boldsymbol{\Psi} = \bar{\boldsymbol{\Omega}}^{\mathsf{T}} \otimes \mathbf{W}^{\mathsf{H}}$. Then, (1.7) can be simplified as $\mathbf{y} = \boldsymbol{\Psi}\mathbf{h}_c + \mathbf{n}$. Based on the obtained signal model, the objective of this work is to extract $\mathbf{h}_c$ from the noisy received signal $\mathbf{y}$ by assuming that the matrix $\boldsymbol{\Psi}$ is known. This is accomplished by using the deep unfolding method, which is detailed next.

1.3.2 Optimization Problem Formulation

In order to recover $\mathbf{h}_c$ from the noisy observation $\mathbf{y}$, we formulate the following regularized optimization problem

$$\hat{\mathbf{h}}_c = \arg\min_{\mathbf{h}_c} \|\mathbf{y} - \boldsymbol{\Psi}\mathbf{h}_c\|_2^2 + \lambda\, \mathrm{rank}(\mathbf{H}_c), \tag{1.9}$$

which takes into consideration the rank deficiency of the cascaded channel $\mathbf{H}_c$ and the impact of noise [18]. The regularization parameter $\lambda > 0$ is introduced to control the tradeoff between the data fitting and the rank of the cascaded channel. The optimization problem in (1.9) can be further reformulated as

$$\hat{\mathbf{h}}_c = \arg\min_{\mathbf{h}_c} \|\mathbf{y} - \boldsymbol{\Psi}\mathbf{h}_c\|_2^2 + \lambda\|\mathbf{H}_c\|_*, \tag{1.10}$$

which is obtained by relaxing $\mathrm{rank}(\mathbf{H}_c)$ with its nuclear norm, i.e., $\|\mathbf{H}_c\|_*$. This is a convenient approach because $\mathrm{rank}(\mathbf{H}_c)$ is a noncovex function of $\mathbf{H}_c$. In addition, $\|\mathbf{H}_c\|_{\mathrm{F}} \leq \|\mathbf{H}_c\|_* \leq \sqrt{r}\|\mathbf{H}_c\|_{\mathrm{F}}$ with $r \geq 1$. Notably, when $\mathrm{rank}(\mathbf{H}_c) = 1$ (e.g., $\mathbf{H}_1$ has only the LoS path), we have $\|\mathbf{H}_c\|_* = \|\mathbf{H}_c\|_{\mathrm{F}}$. Also, the singular values of $\mathbf{H}_c$ have a high probability to fulfill the following condition: $\sigma_1 \gg \sigma_2 > \cdots > \sigma_{L_1}$ with σ_i being the ith largest singular value of $\mathbf{H}_c$, which results in $\|\mathbf{H}_c\|_* \approx \|\mathbf{H}_c\|_{\mathrm{F}}$. Thus, we further replace $\mathrm{rank}(\mathbf{H}_c)$ in (1.10) with $\|\mathbf{H}_c\|_{\mathrm{F}}$, i.e., $\|\mathbf{h}_c\|_2$, which yields

$$\hat{\mathbf{h}}_c = \arg\min_{\mathbf{h}_c} \|\mathbf{y} - \boldsymbol{\Psi}\mathbf{h}_c\|_2^2 + \lambda\|\mathbf{h}_c\|_2. \tag{1.11}$$

To accurately solve this optimization problem, we need to carefully choose the regularization parameter λ. The optimal value of λ is, however, difficult to obtain. As a reference, λ is chosen equal to $4\sigma^2\sqrt{\frac{MN(M+N)\log(M+N)}{N_{\mathrm{W}}K}}$ [18].

1.3.3 Model-Driven Deep Unfolding

Deep unfolding is a deep neural network framework that mimics the conventional gradient descent method. The difference lies in that deep unfolding is able to learn from a large amount of (synthetic) data with enhanced performance and reduced online implementation complexity and number of iterations. Typically, this is exemplified in a reduced number of layers in the deep unfolding network. When solving the optimization problem in (1.11) by using the (conventional) gradient descent method, we iteratively update $\mathbf{h}_c^{(i)}$, with (i) denoting the iteration index, as follows

$$\mathbf{h}_c^{(i)} = \mathbf{h}_c^{(i-1)} - \beta\nabla f(\mathbf{h}_c^{(i-1)}), \tag{1.12}$$

where $0 < \beta < 1$ is the step size and $\nabla f(\mathbf{h}_c^{(i-1)})$ is the gradient of $f(\mathbf{h}_c) = \|\mathbf{y} - \mathbf{\Psi}\mathbf{h}_c\|_2^2 + \lambda\|\mathbf{h}_c\|_2$ evaluated at $\mathbf{h}_c^{(i-1)}$, which can be expressed as

$$\nabla f(\mathbf{h}_c^{(i-1)}) = (\mathbf{\Psi}^{\mathsf{H}}\mathbf{\Psi}\mathbf{h}_c^{(i-1)} - \mathbf{\Psi}^{\mathsf{H}}\mathbf{y}) + \lambda\mathbf{h}_c^{(i-1)}/\|\mathbf{h}_c^{(i-1)}\|_2, \tag{1.13}$$

when λ is fixed. The initial value, i.e, $\mathbf{h}_c^{(0)}$, can be set equal to the all-zero vector. In this case, the denominator $\|\mathbf{h}_c^{(i-1)}\|_2$ in the last term of (1.13) needs to be modified as $\|\mathbf{h}_c^{(i-1)}\|_2 + \epsilon$ with $\epsilon > 0$ when $i = 1$.

Substituting (1.13) into (1.12), we obtain

$$\mathbf{h}_c^{(i)} = \mathbf{h}_c^{(i-1)} - \beta\mathbf{\Psi}^{\mathsf{H}}\mathbf{\Psi}\mathbf{h}_c^{(i-1)} + \beta\mathbf{\Psi}^{\mathsf{H}}\mathbf{y} - \beta\lambda\mathbf{h}_c^{(i-1)}/\|\mathbf{h}_c^{(i-1)}\|_2. \tag{1.14}$$

The Gram matrix $\mathbf{\Psi}^{\mathsf{H}}\mathbf{\Psi}$, the compressed statistics $\mathbf{\Psi}^{\mathsf{H}}\mathbf{y}$, and $\mathbf{h}_c^{(i-1)}$, are needed to apply the gradient descent algorithm. Therefore, these three terms constitute the input variables of the deep unfolding neural network model.

To be specific, the ith layer of the deep unfolding model for mimicking the gradient descent iteration in (1.14) is introduced in Fig. 1.2.

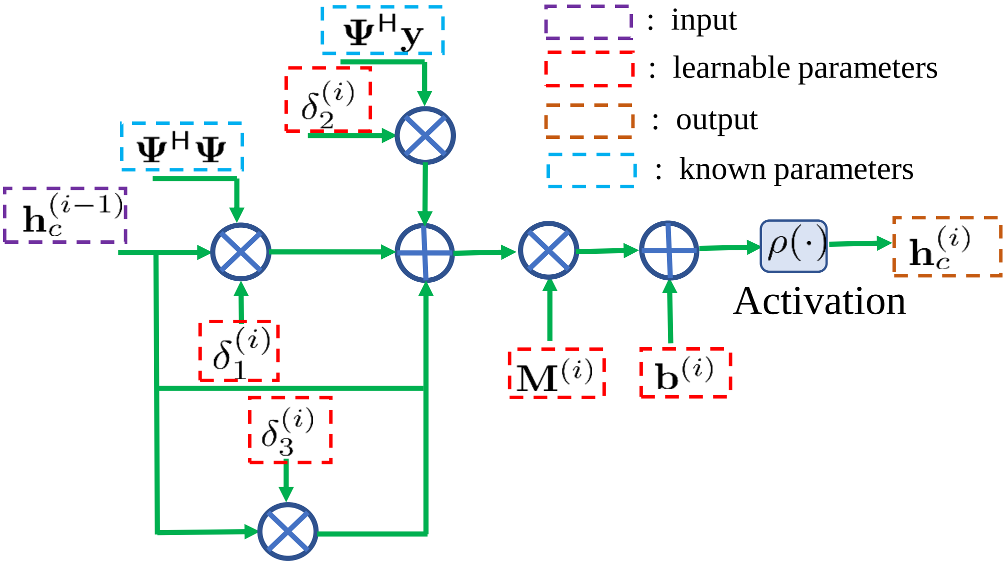

Figure 1.2: The ith layer of the deep unfolding network model for estimating the cascaded channel vector.

The accuracy and convergence speed of the channel estimate in (1.14) highly depends on the specific choice of the step size β and the regularization parameter λ. In the considered deep unfolding model, these parameters are learnable parameters that are automatically determined during the data-driven training phase. To this end, we introduce three generalized learnable parameters $\delta_1^{(i)} \in [-1,\ 0]$, $\delta_2^{(i)} \in [0,\ 1]$, and $\delta_3^{(i)} \in [-1,\ 0]$, for the ith layer of the deep unfolding model in Fig. 1.2. In (1.14), more specifically, $-\beta$ and β in the second and third term are replaced by $\delta_1^{(i)}$ and $\delta_2^{(i)}$, respectively, and the product $-\beta\lambda/\|\mathbf{h}_c^{(i-1)}\|_2$ in the last term is unfolded in the learnable parameter $\delta_3^{(i)}$. As shown in Fig. 1.2, in order to further enhance the prediction capabilities of the deep unfolding network model, we serially concatenate the term

$\mathbf{h}_c^{(i-1)} + \delta_1^{(i)} \mathbf{\Psi}^{\mathsf{H}} \mathbf{\Psi} \mathbf{h}_c^{(i-1)} + \delta_2^{(i)} \mathbf{\Psi}^{\mathsf{H}} \mathbf{y} + \delta_3^{(i)} \mathbf{h}_c^{(i-1)}$ with a learnable weight matrix $\mathbf{M}^{(i)}$, a bias vector $\mathbf{b}^{(i)}$, and a non-linear activation function.

The complete deep unfolding network model is illustrated in Fig. 1.3 and it comprises L layers from Fig. 1.2. In particular, the observations $\{\mathbf{\Psi}^{\mathsf{H}}\mathbf{\Psi}, \mathbf{\Psi}^{\mathsf{H}}\mathbf{y}\}$ are input to all the layers of the deep unfolding network model. The online computational complexity of the proposed scheme is $\mathcal{O}(M^2N^2L)$, which is smaller than the ANM based scheme that requires $\mathcal{O}((M+N)^6)$ per iteration [9]. In the later studied case with $M = 16, N = 32$, we have $M^2N^2L \ll (M+N)^6 L$ by assuming that L iterations are needed for ANM as well.

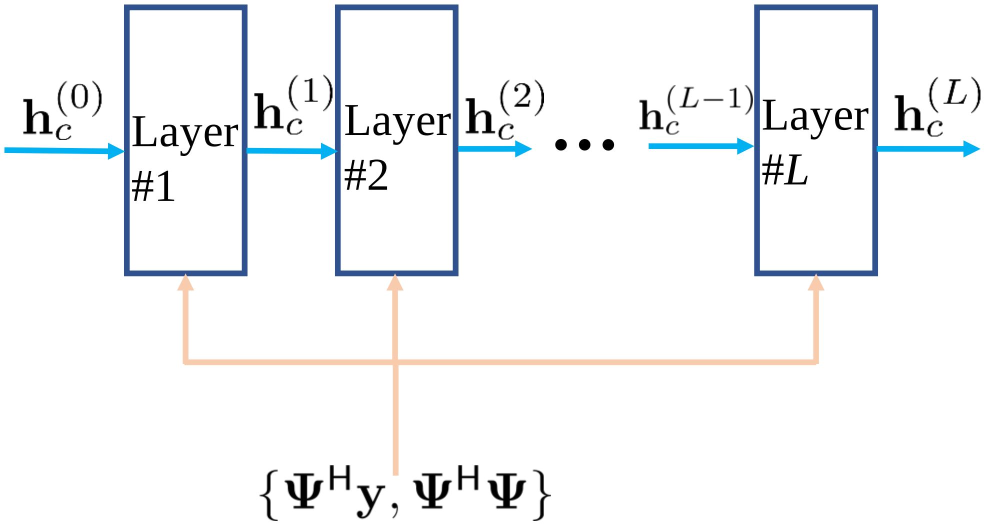

Figure 1.3: Complete deep unfolding network model for channel estimation, which comprises L layers from Fig. 1.2

1.4 Numerical Results

In this section, we evaluate the performance of the proposed deep unfolding network model against two benchmark schemes: (i) the LS estimator and (ii) the direct solution of (1.11) by using the CVX toolbox.[3] We evaluate the impact of the training overhead, the training SNR, the number of paths, and the angular parameter distribution. As far as the RIS phase control matrices as concerned, their diagonal elements are set equal to the column vectors of a discrete Fourier transform (DFT) matrix. A set of orthonormal vectors are considered for $\mathbf{W}$, e.g., the normalized column vectors from a DFT matrix. It is worth mentioning that we transform the data from the complex-valued domain to the real-valued domain before applying the deep unfolding network model. The channel $\mathbf{h}_c^{(0)}$ is set equal to the all-zero vector. In the first $L-1$ layers, we use *relu* activation functions, while no activation function is applied in the last layer. The loss function during the training phase is the NMSE between the output cascaded channel vector and the ground-truth cascaded channel vector. The *Adam* algorithm is used for training, whose learning rate is 0.001 during the first 20 epochs and it is halved in the

---

[3] The scripts of the implementation are available at https://github.com/jiguanghe/RISCE.

remaining epochs, and the batch size is 64. We use $1e5$ samples for training and $1e4$ samples for testing. The parameter setup is summarized in Table 1.1.

In the sequel, we study the impact of the training overhead, the number of paths, the training SNR, and the angular parameter distribution on the estimation performance in detail.

Table 1.1: Parameter Setup.

Parameter	Value	Parameter	Value
L_1	$\{1, 2, 3\}$	$\mathbf{h}_c^{(0)}$	$\mathbf{0}$
L_2	$\{1, 2, 3\}$	Optimizer	*Adam*
σ^2_{LoS}	1	Learning rate	$0.001, 0.0005$
σ^2_{NLoS}	0.01	Batch size	64
M	16	$\rho(\cdot)$	*relu*
N	32	Training samples	$1e5$
L	15	Testing samples	$1e4$
$\sin(\boldsymbol{\theta}_1)$	$\mathcal{U}[0,\ 1]$	Loss	NMSE
$\sin(\boldsymbol{\phi}_1)$	$\mathcal{U}[0,\ 1]$	$\sin(\boldsymbol{\phi}_2)$	$\mathcal{U}[0,\ 1]$
N_{W}	8	K	$\{24, 28\}$

1.4.1 Impact of the Training Overhead

Fig. 1.4 shows the NMSE for a 1×16 SIMO system (i.e., $M = 16$) by using the proposed deep unfolding approach as a function of the training overhead. During the training phase, the SNR is $\gamma = 1/\sigma^2 = 20$ dB. From Fig. 1.4, we see that the proposed scheme with $K = 24$ channel uses for training outperforms the LS estimator even if the latter uses a longer training phase with $K = 32$. Also, as expected, the higher the training overhead is, the lower the NMSE of the proposed scheme is. It is worth noting that the proposed deep unfolding method outperforms the numerical solution of (1.11) by using CVX, and the ANM algorithm. This is attributed to the learning capability of the deep unfolded network through the learnable parameters introduced in Fig. 1.2.[4]

1.4.2 Impact of the Number of Paths

In this subsection, we study the impact of the number of paths, which is increased from one to two and three. The SNR for training is $\gamma = 20$ dB and $K = 28$. The corresponding NMSE is shown in Fig. 1.5. When the number of paths increases, the rank of the cascaded channel increases accordingly. In this case, Fig. 1.5 shows that the NMSE increases as the number of paths increases. In other words, by keeping the

---

[4] If the regularization parameter λ in (1.11) can be optimally designed, better performance can be expected. However, finding the optimal λ is still an open problem.

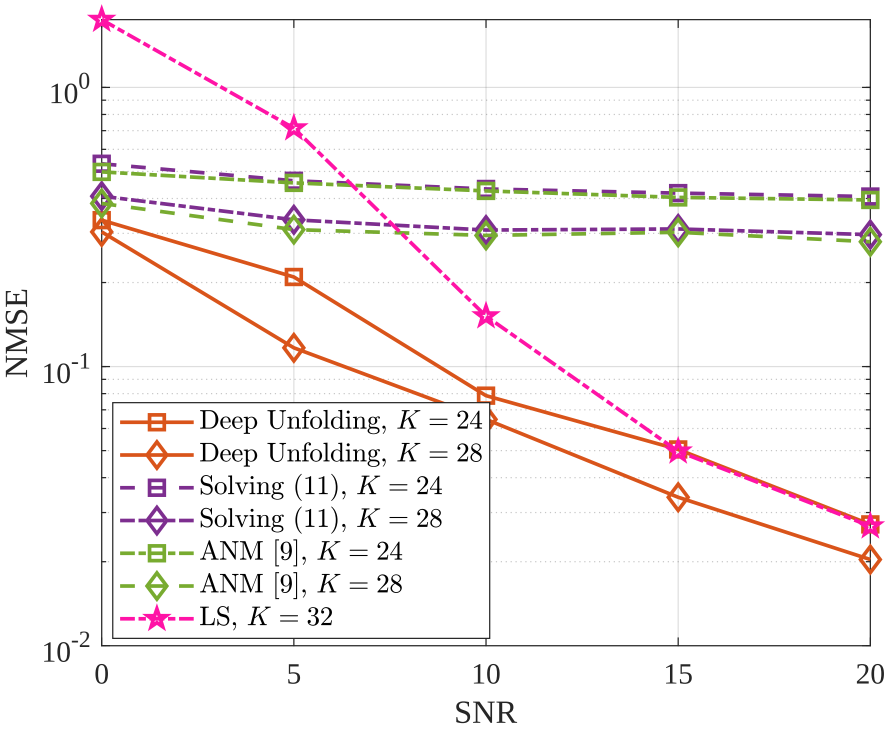

Figure 1.4: Impact of training overhead on estimating the cascaded channel for a 1×16 SIMO system with $N = 32$ and $L_1 = L_2 = 1$. Deep unfolding vs. LS estimation, ANM [9], and the direct solution of (1.11) [18].

training overhead fixed, the proposed deep unfolding method benefits from the sparsity of the channel, i.e., the number of paths is small.

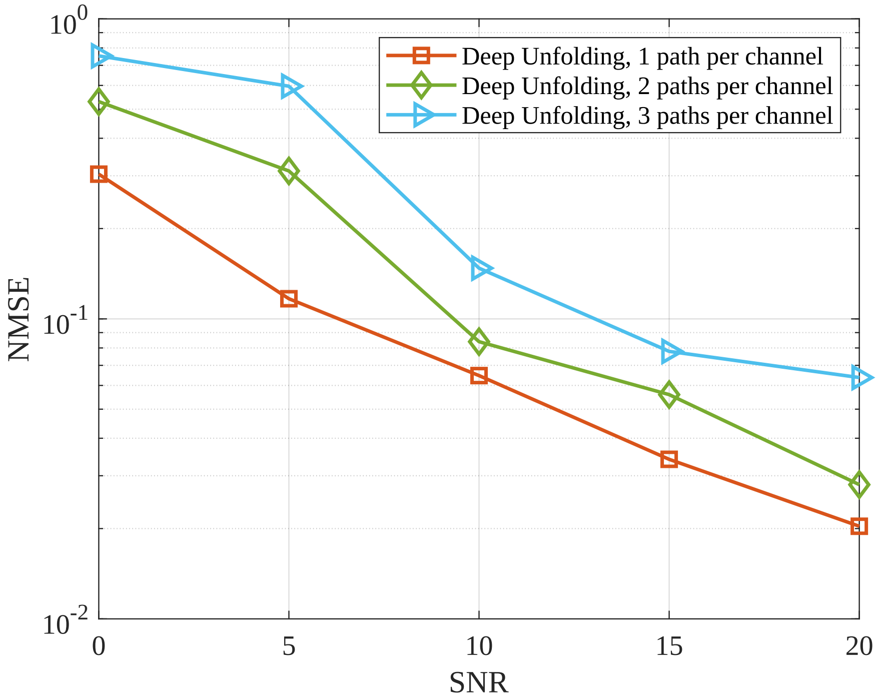

Figure 1.5: Impact of the number of paths on estimating the cascaded channel for a 1×16 SIMO system with $N = 32$.

1.4.3 Impact of the Training SNR

In this subsection, we study the impact of the training SNR on the estimation performance. Two SNR values, i.e., $\gamma = 0$ dB, $\gamma = 20$ dB, and an SNR that varies in the set $\gamma \in \{0, 5, 10, 15, 20\}$ dB are considered. The corresponding NMSE is shown in Fig. 1.6. We observe that the proposed deep unfolding method provides the best NMSE when it is trained at a high SNR except if the operating SNR during the test phase is too low. In other words, nearly noise-free training samples bring the best performance in the high SNR regime, and vice versa, as depicted in Fig. 1.6. Since the data are generated in real-time according to the statistics of the channels and noises, the performance in terms of NMSE may not always decrease as a function of SNR. This may be caused by the fact that the trained model is more suitable for certain SNR values (e.g., high SNR with almost noise-free training samples) than others. Intuitively, the training SNR plays a critical role in the prediction performance of the deep unfolding models.[5]

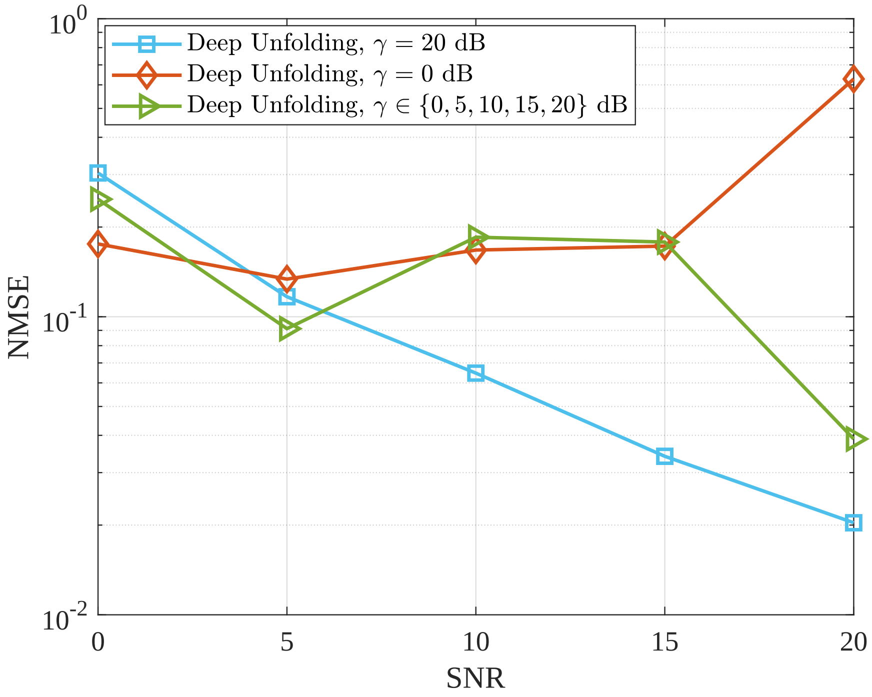

Figure 1.6: Impact of the training SNR on estimating the cascaded channel for a 1×16 SIMO system with $N = 32$.

1.4.4 Impact of the Angular Parameter Distribution

Unlike the previous study in which the angular parameters are distributed as $\mathcal{U}[0,\ 1]$, in this subsection, we evaluate the impact of the angular parameter distribution when estimating the cascaded channel. The corresponding NMSE is shown in Fig. 1.7. We observe that the NMSE decreases when the range of $\sin(\boldsymbol{\theta}_1), \sin(\boldsymbol{\phi}_1), \sin(\boldsymbol{\phi}_2)$ decreases. In other words, the estimation accuracy of the proposed deep unfolding method increases when the individual channels are subject to a reduced variability.

---

[5] If the SNR value(s) can be incorporated into the proposed deep unfolding structure, better performance is expected, which is left for our future investigation.

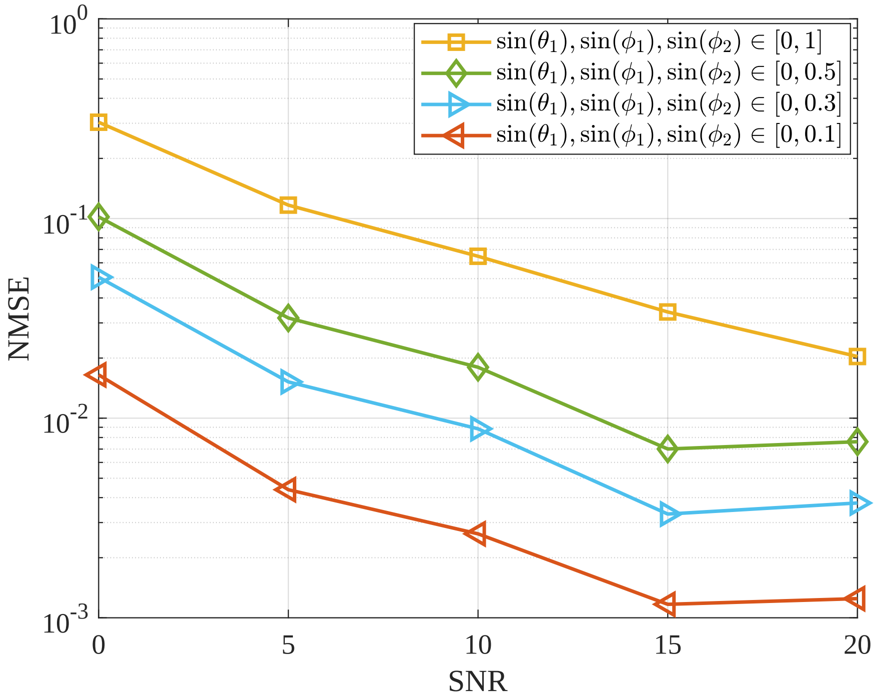

Figure 1.7: Impact of the angular parameter distribution on estimating the cascaded channel for a 1×16 SIMO system with $N = 32$.

1.5 Conclusion

In this chapter, we have introduced a deep unfolding model for efficiently estimating the end-to-end RIS channel in SIMO systems. With the aid of simulation results, we have shown that the proposed approach can outperform three benchmark schemes based on the LS method, a CVX-based numerical solution of the channel estimation problem, and the ANM algorithm. The impact of the number of paths, the training SNR, and the angular parameter distribution on the estimation accuracy has been investigated. In addition, the proposed deep unfolding network model has a low online prediction complexity, since it requires the computation of vector matrix multiplications and additions. On the other hand, the LS estimation methods usually require a matrix inversion.

Chapter 2

Autonomous Reconfigurable Intelligent Surfaces Through Wireless Energy Harvesting

2.1 Introduction

As the wireless world moves towards the sixth-generation (6G) era, the data-rate demands exponentially increase. To prevent a possible capacity crunch, one candidate solution that has been put forward is the migration to frequency bands in the millimeter-wave, sub-terahertz, and terahertz (THz) range [19]. However, the higher blockage susceptibility in those bands make the coverage patchy. To overcome this issue, active relaying and the use of passive reflectors, such as dielectric mirrors, have been proposed. However, the main drawback of active relaying is need for a dedicated power supply for amplification, while the drawback of passive reflectors is their limited impact on the coverage due to the inability to dynamically control the reflection angle [20]. A promising solution that combines the benefits of both technologies without their disadvantages has been brought forward by the reconfigurable intelligent surfaces (RISs) paradigm [21–23].

RISs are artificial structures consisting of a dielectric substrate that embeds conductive elements, named reflective units (RUs), of sub-wavelength size and distance between adjacent elements. Typical RUs are comprised of either dipoles, patches, or string resonators, indicatively. By properly tuning their impedance through the use of semiconductor components, such as positive-intrinsic-negative (PIN) diodes, field-effect transistors (FETs), and radio-frequency micro-electromechanical systems (RF-MEMS), their amplitude and phase response, with respect to an impinging electromagnetic wave, can be altered. Hence, besides reflecting an impinging beam towards an arbitrary direction or point, they can also act as absorbers of the impinging electromagnetic energy. In addition, an amount of power is needed for their reconfigurability, but not during a constant reflection configuration [22]. This is the reason why the RIS operation has been characterized as *nearly passive*. If the reconfiguration is infrequent, the power consumption is arguably smaller than when operating an active relay.

With respect to RIS deployment in communication networks, there has been an intensive investigation in various domains [21]. In addition, when compared to active relaying, which also allows beamforming in an arbitrary direction, several works showcase that sufficiently large RISs can in fact outperform their relay counterparts [22, 24–26].

An important question that the RIS's nearly-passive feature raises is whether they can achieve power autonomy by covering their needs through wireless energy harvesting. The vast majority of RIS related works dealing with wireless power transfer employ the RISs for assisting the transfer of power to end users and not for powering the RISs [27], [28]. To the best of our knowledge, only [29] and [30] consider wirelessly powered RISs. However, the related works lack RIS power consumption and energy harvesting models nor introduce the RIS electronic modules that drive its power consumption. This is essential towards the identification of the advances needed in ultra-low power electronics that can realize the vision of autonomous RISs. Motivated by this, the contribution of this chapter can be summarized as follows:

- We present a comprehensive RIS power consumption model that captures its main power-consuming electronic components.
- We propose an energy harvesting model that is used for extracting the RIS harvested power and for formulating the optimization problem of interest. In particular, we focus on the optimal RIS placement as well as the amplitude and phase response adjustment of the RUs for maximizing the end-to-end signal-to-noise ratio (SNR), subject to the harvested power being sufficient for RIS autonomous operation.
- An analytical solution is provided for the amplitude and phase response optimal values of the RUs.
- Through the simulations, we provide a range of average power consumption of the RIS electronics that guarantees its autonomous operation.

2.2 System Model and Power-Consuming Modules

In this section, we present the system model under consideration and identify the RIS modules that consume power.

2.2.1 System Model

As illustrated in Fig. 2.1, we consider a fixed-topology street-level scenario in which a transmitter (TX) communicates with a receiver (RX) through an RIS located in the far field of both the TX and RX. Additional, $r_{1,h}$, $r_{2,h}$, and r_h denote the horizontal TX-RIS, RIS-RX, and TX-RX distances, respectively, while h_t, h_s, and h_r are the TX, RIS, and RX heights, respectively. The incidence and departure angles of the electromagnetic wave with respect to the center of the illuminated area (RIS center) are respectively denoted by θ_i and θ_r. The considered TX-RIS and RIS-RX blockage-free links constitute an alternative path to the direct TX-RX link that is assumed to be blocked. Such a scenario can be a typical future street-level fronthaul/backhaul setup. To countermeasure the high pathloss in such bands, both the TX and RX are equipped with highly

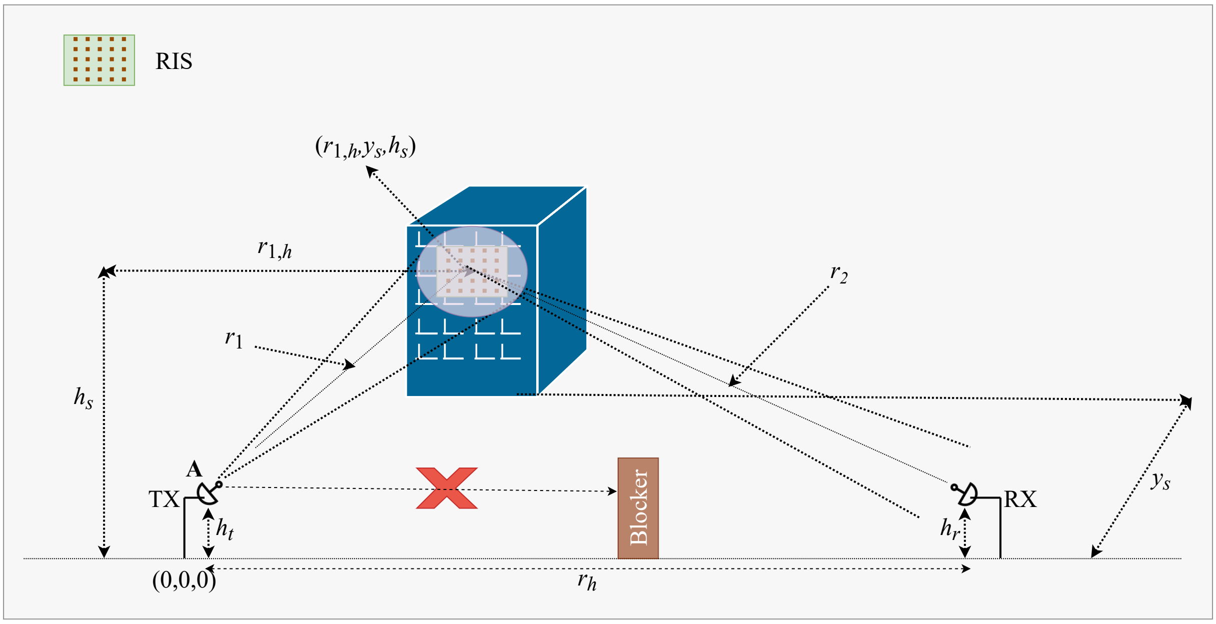

Figure 2.1: Illustration of the system model and notation.

directional antennas. We consider parabolic antennas with diameters D_t and D_r, respectively. As a result, their maximum gain, denoted by G_m^{max}, $m \in \{t, r\}$, for $D_t, D_r \gg \lambda$, where λ represents the wavelength, is given by [31]

$$G_m^{\max} = e_m \left(\frac{\pi D_m}{\lambda} \right)^2, \quad m \in \{t, r\}, \tag{2.1}$$

where e_m is their efficiency. Note that this type of antennas has been extensively used for wireless backhaul/fronthaul scenarios (see [32] and reference therein), due to their capability to support pencil-beamforming transmissions. In addition, we assume that the TX and RX antennas are pointing towards the center of the illuminated RIS region so the maximum gain is achieved. Furthermore, we note that even in such fixed-topology scenarios the RISs need to be occasionally reconfigured such as in the case of backhaul links in a mesh architecture [33].

We assume that the RIS has been deployed to have a line-of-sight path to the TX and RX. As far as the channel model is concerned, for both the TX-RIS and RIS-RX channels, we assume that the direct path dominates (as it has been reported through measurements in the mmWave bands [34]) and use the free-space propagation model.

The RIS, consisting of $M_s = M_x \times M_y$ RUs of size $d_x \times d_y$, is configured to act as a beamformer, which, by proper adjustment of the RU phase response, is capable of steering an incident wave from any direction towards the angular direction θ_r to the RX direction. Each RU is an electrically-small low-gain element with gain pattern that can be expressed as [31]

$$G_s(\theta) = 4\cos(\theta), \text{ with } 0 \leq \theta < \pi/2. \tag{2.2}$$

Moreover, it is assumed that the transmission power is P_t and that the received signal is subject to additive white complex Gaussian noise with power σ^2 [31], computed in dBm as

$$\sigma^2 = -174 + 10\log_{10}(W) + \mathcal{F}_{\mathrm{dB}}, \tag{2.3}$$

where $\mathcal{F}_{\mathrm{dB}}$ is the noise figure in dB and W is the bandwidth.

Remark 1. *The assumption of a fixed-topology scenario does not preclude the validity of the outcomes of this work also for mobile scenarios. In particular, we can envisage a future urban scenario abundant in RISs that are mounted on fixed structures, such as buildings. In such a case, the equivalent question that can be answered by the results of this work is which RIS should be chosen in order to maximize the SNR subject to the harvested power being sufficient for RIS autonomous operation. In such a case, we can still assume that the free-space TX-RIS-RX propagation model approximately applies considering the elevation of the RIS with respect to the positions of the TX and RX.*

2.2.2 RIS Power-Consuming Modules

Impedance-adjusting semiconductor components This power consumption is characterized by two factors, namely the static power consumption and the dynamic power consumption. The first factor corresponds to their continuous power consumption due to leakage currents originating from the bias voltages when they operate in steady state. Usually, the resulting direct-current (DC) power consumption is virtually negligible for FETs and RF MEMS. [35]. On the other hand, the dynamic power consumption constitutes a non-negligible factor related to the charging and discharging of internal capacitors during bias voltage level changes needed for RU phase and amplitude response adjustment. It is present only when the semiconductor components change state, which means that its effect is alleviated in low-mobility scenarios.

Energy-harvesting modules For the RF-to-DC power conversion that is needed to power the RIS semiconductor components, we consider corporate feed networks in which the accumulated energy by a group of RUs is driven to a single rectifying circuit instead of dedicating one rectifying circuit per RU [36]. The rectifying circuits can be either passive that exhibit negligible power consumption or can be active by incorporating active diodes that increase the conversion efficiency, but result in a non-negligible power consumption.

Control network As described in [37], the RIS needs to receive external commands regarding the configuration state it needs to assume. This can be achieved by either of two basic approaches: i) detached microcontroller architecture; ii) integrated architecture. In this work, we consider the integrated architecture since it has a strong potential for enabling autonomous RIS operation due to expected low power consumption, as suggested by [37]. In such an architecture, the reconfiguration requests that are wirelessly received by the RIS are dispatched to an integrated network of communicating chips, which involve controllers that read the RU state and adjust the bias voltages of the impedance-adjusting semiconductor elements. The chip circuits that receive, interpret, and apply the commands exhibit their own static and dynamic power consumption due to leakage and transistor switching, respectively [38]. In addition, they are likely to use asynchronous logic due to the resulting small power consumption [39].

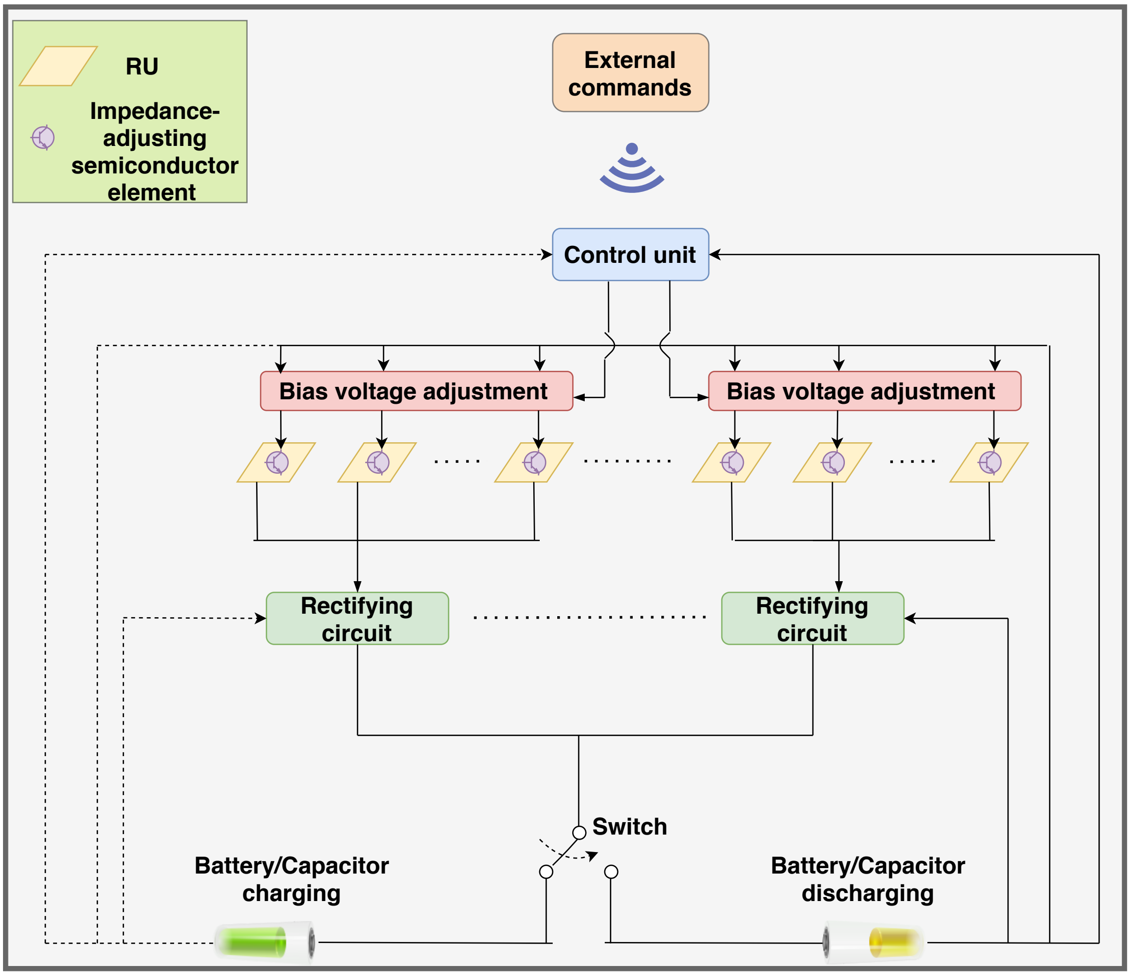

Figure 2.2: The proposed energy harvesting model.

2.3 RU Reflection Coefficient, Energy-Harvesting, and Power Consumption Models

In this section, we first present the considered model for the RU reflection coefficient and, subsequently, the energy-harvesting together with the power consumption model.

2.3.1 RU Reflection-Coefficient Model

We assume that the phase $\varphi_{p,l}$ and amplitude $A_{p,l}$ response of the (p,l)th RU can be tuned independently from each other. Although the RU phase and amplitude response are physically coupled [40], there are design approaches that substantially alleviate such an inter-dependency [41]. Hence, the proposed model can serve as an upper bound on the achievable performance.

2.3.2 Energy Harvesting Model

Our proposed energy harvesting model is depicted in Fig. 2.2. We assume that each RU can act as both an energy harvester and as a reflector of the impinging electromagnetic radiation. The fraction of power that is absorbed (excluding the ohmic and other losses) is equal to $1 - A_{p,l}^2$, while the fraction of reflected power is $A_{p,l}^2$. As depicted in Fig. 2.2, the amount of RF energy that is absorbed by a group of RUs is converted into DC electricity through a rectifying circuit. The total DC energy output of the rectifying circuits charges one of two batteries/capacitors depicted in Fig. 2.2. While one is charging, the other is discharging by providing power supply to both the controller chips that adjust the response of the RUs and the rectifying circuits. Once one of the batteries/capacitors is charged and the other one is discharged,[1] the switch depicted in Fig. 2.2 swaps between them.

2.3.3 Power Consumption Model

For the RIS power consumption, denoted by P_{RIS}, by assuming one chip per RU it holds[2]

$$P_{\text{RIS}} = M_s\, P_c + M_{\text{rect}}\, P_{\text{rect}}, \tag{2.4}$$

where with P_c we incorporate both the power consumption of the control chip and the one of the impedance adjusting semiconductor component. Futhermore, P_{rect} is the power consumption of each of the M_{rect} rectifying circuits. We can consider P_c as an equivalent continuous power consumption level (average value). For example, by denoting the static power consumption of the chip as P_{static}, its dynamic one as P_{dynamic}, and the percentage of time that the RIS needs to be reconfigured (this depends on the switching frequency and the reconfiguration duration) by p_r, it holds that

$$P_c = P_{\text{static}} + p_r P_{\text{dynamic}}. \tag{2.5}$$

2.4 Problem Formulation and Solution

In this section, we first compute the SNR and, subsequently, we present the total harvested RIS power model. Finally, we formulate and solve the optimization problem of interest.

2.4.1 Signal-to-Noise Ratio

The SNR at the RX, which is given by

$$\rho_s = \left(\frac{\lambda}{4\pi}\right)^4 \frac{P_t G_t^{max} G_r^{max} G_s\left(\theta_i\right) G_s\left(\theta_r\right)}{r_1^2 r_2^2 \sigma^2} \left| \sum_{p=1}^{M_x} \sum_{l=1}^{M_y} A_{p,l} \exp\left(-j\left(\varphi_{p,l} + \frac{2\pi\left(r_{1_{p,l}} + r_{2_{p,l}}\right)}{\lambda}\right)\right)\right|^2 . \tag{2.6}$$

---

[1] Assuming, ideally, the same charging and discharging rates.

[2] The assumed linear dependency of the power consumption on the number of electronic chips $(M_s P_c)$ can be considered as an upper bound on the amount that is expected in practice. This is due to the fact that the percentage of the electronic chips contributing to a steering angle change depends on the previous and targeted angle [42].

This formula can be obtained by following similar steps as in [31, Appendix C]. The parameters $r_{1_{p,l}}$ and $r_{2_{p,l}}$ are the distances between the TX center and the (p, l) element, and between the (p, l) element, and the RX center, respectively, given by

$$r_{1_{p,l}} = \sqrt{\left(r_{1,h}-d_p\right)^2+y_s^2+\left(h_s-h_t-d_l\right)^2}, \; r_{2_{p,l}} = \sqrt{\left(r_{1,h}-d_p\right)^2+y_s^2+\left(h_s-h_t-d_l\right)^2}. \tag{2.7}$$

where d_p and d_l denote the distances between the RIS center and the (p, l) RU in the x- and y-axis, respectively. Furthermore, r_1 and r_2 are the distances between the TX and the RIS center and between the RIS and RX center, respectively. They are given by

$$r_1 = \sqrt{r_{1,h}^2+y_s^2+\left(h_s-h_t\right)^2}, \; r_2 = \sqrt{\left(r_h-r_{1,h}\right)^2+y_s^2+\left(h_s-h_r\right)^2}. \tag{2.8}$$

Moreover, θ_i and θ_r are given by

$$\theta_i = \tan^{-1}\left(\frac{\sqrt{r_{1,h}^2+\left(h_s-h_t\right)^2}}{y_s}\right), \tag{2.9}$$

$$\theta_r = \tan^{-1}\left(\frac{\sqrt{\left(r_{1,h}-r_h\right)^2+\left(h_s-h_r\right)^2}}{y_s}\right). \tag{2.10}$$

2.4.2 RIS Harvested Power Model

The absorbed power of the (p, l) RU element, which we denote by $P_{abs_{p,l}}$, can be obtained as

$$P_{\mathrm{abs}_{p,l}} = \left(1-A_{p,l}^2\right) P_{i_{p,l}} = \left(\frac{\lambda}{4\pi}\right)^2 \frac{P_t \left(1-A_{p,l}^2\right) G_t^{max} G_s\left(\theta_i\right)}{r_1^2}. \tag{2.11}$$

Hence, the total absorbed power of the RIS per communication time slot is the sum of $P_{\mathrm{abs}_{p,l}}$ across all RUs. We let $\epsilon_{\mathrm{conv}} \in (0, 1)$ the RF-DC conversion efficiency, which is the same for all the employed rectifying circuits. The total harvested power from the RIS is then given by

$$P_{\mathrm{harv}} = \epsilon_{\mathrm{conv}} \sum_{p=1}^{M_x} \sum_{l=1}^{M_y} P_{\mathrm{abs}_{p,l}}. \tag{2.12}$$

For enabling the perpetual (autonomous) operation of the RIS, it should hold that $P_{\mathrm{harv}} \geq P_{\mathrm{RIS}}$. By plugging (2.2), (2.8), and (2.9) into (2.11), P_{harv} as a function of $r_{1,h}$ and $\mathbf{A} = \left\{A_{p,l}\right\}$ is given by

$$P_{\mathrm{harv}}\left(r_{1,h}, \mathbf{A}\right) = 4\epsilon_{\mathrm{conv}} \left(\frac{\lambda}{4\pi}\right)^2 P_t G_t^{max} \sum_{p=1}^{M_x} \sum_{l=1}^{M_y} \frac{1-A_{p,l}^2}{r_{1,h}^2+y_s^2+\left(h_s-h_t\right)^2} \cos\left(\tan^{-1}\left(\frac{\sqrt{r_{1,h}^2+\left(h_s-h_t\right)^2}}{y_s}\right)\right). \tag{2.13}$$

2.4.3 Problem Formulation and Solution

The problem of interest is formulated as

$$\begin{aligned} \underset{r_{1,h},\mathbf{A},\varphi}{\text{maximize}} \quad & \rho_s\left(r_{1,h},\mathbf{A},\varphi\right) \\ \text{subject to} \quad & P_{\text{harv}}\left(r_{1,h},\mathbf{A}\right) = P_{\text{RIS}},\ 0 < A_{p,l} < 1, \end{aligned} \tag{2.14}$$

where $\varphi = \left\{\varphi_{p,l}\right\}$ and $\rho_s\left(r_{1,h},\mathbf{A},\varphi\right)$ is given by

$$\begin{aligned} \rho_s\left(r_{1,h},\mathbf{A},\varphi\right) = 16 P_t G_t^{max} G_r^{max} \left(\frac{\lambda}{4\pi}\right)^4 \frac{\cos\left(\tan^{-1}\left(\frac{\sqrt{r_{1,h}^2+(h_s-h_t)^2}}{y_s}\right)\right)\cos\left(\tan^{-1}\left(\frac{\sqrt{\left(r_{1,h}-r_h\right)^2+(h_s-h_r)^2}}{y_s}\right)\right)}{\left(r_{1,h}^2+y_s^2+(h_s-h_t)^2\right)\left(\left(r_h-r_{1,h}\right)^2+y_s^2+(h_s-h_r)^2\right)\sigma^2} \\ \times\left|\sum_{p=1}^{M_x}\sum_{l=1}^{M_y} A_{p,l}\exp\left(-j\left(\varphi_{p,l}+\frac{2\pi\left(r_{1_{p,l}}\left(r_{1,h}\right)+r_{2_{p,l}}\left(r_{1,h}\right)\right)}{\lambda}\right)\right)\right|^2. \end{aligned} \tag{2.15}$$

By employing (2.2), (2.8), (2.9), and (2.10) into (2.6). As a constraint for the harvested power, we consider that it should be equal to the required amount needed to power the RIS electronics and not larger in order to devote more power to the information transmission.

For the optimal values of $\varphi_{p,l}$, $A_{p,l}$, and $r_{1,h}$, denoted by $\varphi^*_{p,l}$, $A^*_{p,l}$, and $r^*_{1,h}$, respectively, it holds that

$$\varphi^*_{p,l} = -\frac{2\pi\left(r_{1_{p,l}}+r_{2_{p,l}}\right)}{\lambda}, \tag{2.16}$$

$$A^*_{p,l} = \sqrt{1-\frac{P_{\text{RIS}}\left(\left(r^*_{1,h}\right)^2+y_s^2+(h_s-h_t)^2\right)}{4M_s\epsilon_{\text{conv}}\left(\frac{\lambda}{4\pi}\right)^2 P_t G_t^{max}\cos\left(\tan^{-1}\left(\frac{\sqrt{\left(r^*_{1,h}\right)^2+(h_s-h_t)^2}}{y_s}\right)\right)}} \tag{2.17}$$

and $r^*_{1,h}$ is the value of $r_{1,h}$ that maximizes $G\left(r_{1,h}\right)$, given by

$$\begin{aligned} G\left(r_{1,h}\right) = \frac{\cos\left(\tan^{-1}\left(\frac{\sqrt{r_{1,h}^2+(h_s-h_t)^2}}{y_s}\right)\right)\cos\left(\tan^{-1}\left(\frac{\sqrt{\left(r_{1,h}-r_h\right)^2+(h_s-h_r)^2}}{y_s}\right)\right)}{\left(r_{1,h}^2+y_s^2+(h_s-h_t)^2\right)\left(\left(r_h-r_{1,h}\right)^2+y_s^2+(h_s-h_r)^2\right)\sigma^2} \\ \times\left(1-\frac{P_{\text{RIS}}\left(r_{1,h}^2+y_s^2+(h_s-h_t)^2\right)}{4M_s\epsilon_{\text{conv}}\left(\frac{\lambda}{4\pi}\right)^2 P_t G_t^{max}\cos\left(\tan^{-1}\left(\frac{\sqrt{r_{1,h}^2+(h_s-h_t)^2}}{y_s}\right)\right)}\right). \end{aligned} \tag{2.18}$$

Proof: The proof is provided in the appendix. ■

2.5 Numerical Results

We consider the parameter values of Table 2.1. In Fig. 2.3, we depict the optimal SNR, denoted by ρ_s^*, obtained by the optimal RIS placement, together with $r_{1,h}^*$ and $A_{p,l}^*$ versus P_c for three values of y_s. From Fig. 2.3(a), we observe that the higher P_c is, the lower ρ_s^* becomes until the RIS's power consumption cannot be covered by harvesting. In addition, we observe that as y_s increases, the range of P_c for which autonomous operation can be sustained is smaller. This is due to the higher TX-RIS distance.

Furthermore, from Fig. 2.3(b), we observe that the higher P_c is, the closer to the TX the RIS needs to be placed. This trend is justified as follows: For relatively small values of P_c, the vast majority of the propagating energy should be dedicated to the SNR maximization since the RIS power needs can be covered by just a small amount of that energy, as it is verified by Fig. 2.3(c). In such a case, the optimal RIS location could, depending on the configuration, be even closer to the middle of the TX-RX distance than the TX, especially for large y_s, as it is verified in [31]. On the other hand, for notable P_c values, the RIS inevitably needs to be placed very close to the TX so that the highest possible amount of energy is harvested, as it is again verified by Fig. 2.3(c).

Table 2.1: Parameter values used in the simulation.

Parameter	Value	Parameter	Value
P_t	1 W	M_{rect}	100
P_{rect}	0 (passive rectification)	h_s	12 m
r_h	100 m	h_t, h_r	3 m
W	2 GHz	D_t, D_r	30 cm
$\mathcal{F}_{\text{dB}}$	10 dB	e_t, e_r	0.7
M_x, M_y	50	e_{conv}	0.6

2.6 Conclusion

The case for RIS-aided communications, compared to active relaying, relies on the belief that the power consumption can be made lower. However, if the RIS still requires a wired power supply, the power reduction might be practically insignificant. The purpose of this work was to determine under which conditions, in terms of placement and element response, an autonomous RIS operation through energy harvesting from information signals is possible. The numerical results reveal that this is indeed possible if the average power consumption of the RIS electronic components does not exceed few microwatts. While the SNR over an RIS-aided communication link is the same when the TX and RX switch roles, the same does not apply for energy harvesting: the RIS should be close to the transmitter. The results from this study can help the system designer to identify the design requirements of future ultra-low power components in order to materialize such a vision.

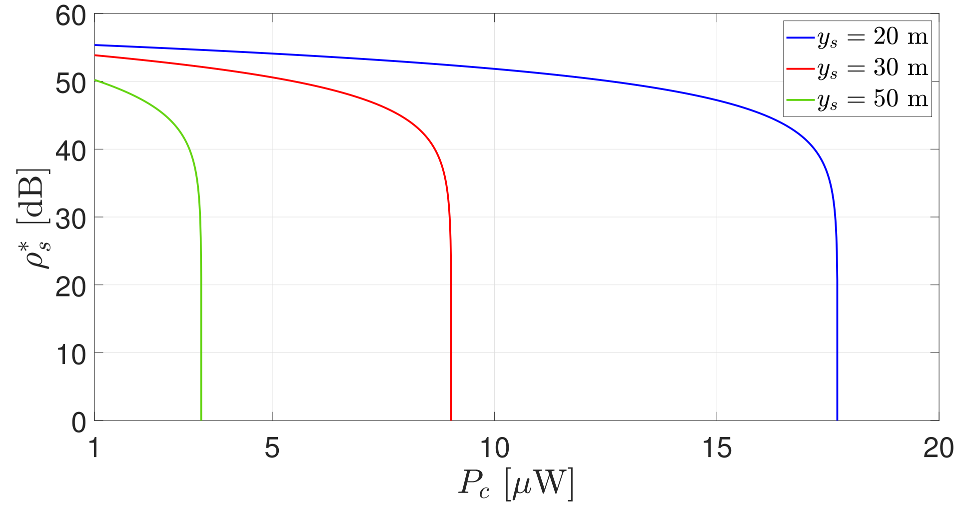

(a) ρ_s^* vs. P_c.

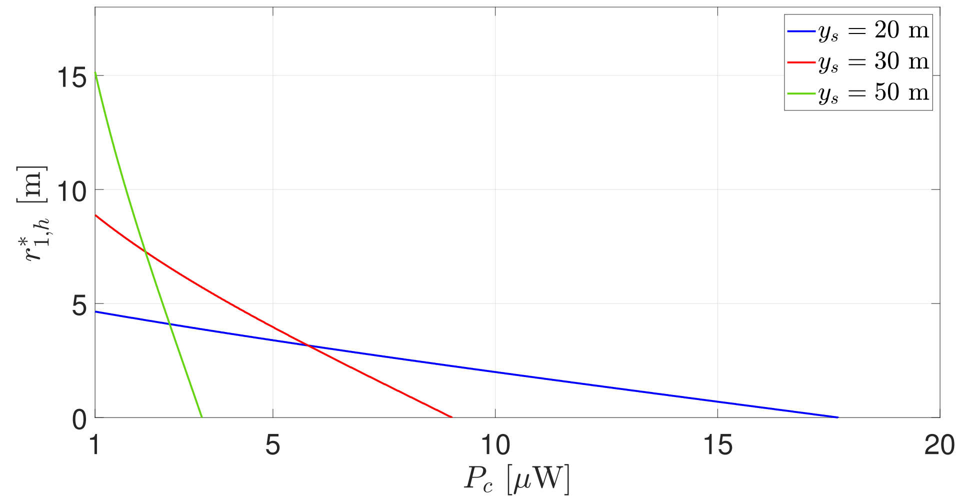

(b) $r_{1,h}^*$ vs. P_c.

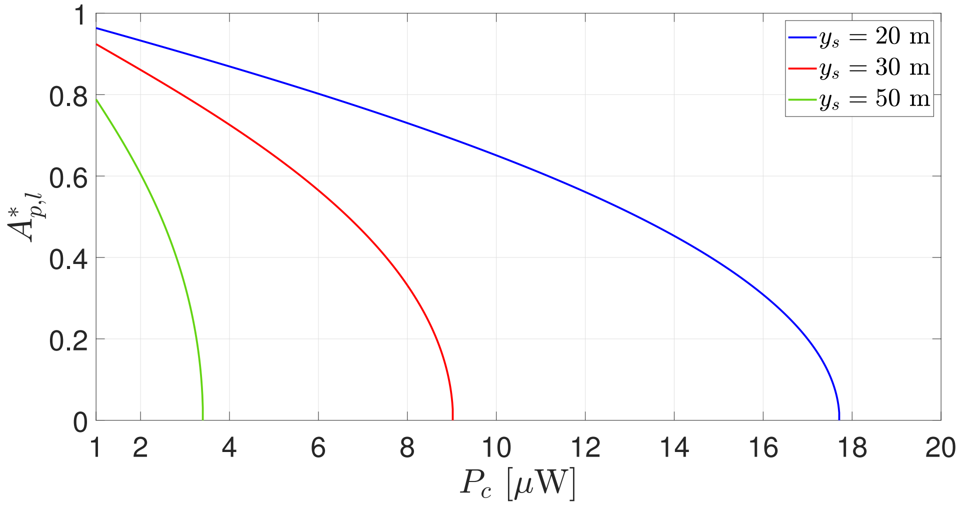

(c) $A_{p,l}^*$ vs. P_c.

Figure 2.3: ρ_s^*, $r_{1,h}^*$, and $A_{p,l}^*$ vs. P_c.

Appendix

We notice that (2.15) is maximized when the complex terms in the norm are co-phased, which is achieved by (2.16). Hence, by plugging (2.16) into (2.15), (2.14) becomes

$$\begin{aligned}&\underset{r_{1,h},A_{p,l}}{\text{maximize}}\ F\left(r_{1,h}\right)\left(\sum_{p=1}^{M_x}\sum_{l=1}^{M_y}A_{p,l}\right)^2\\&\text{subject to}\ H\left(r_{1,h}\right)\sum_{p=1}^{M_x}\sum_{l=1}^{M_y}A_{p,l}^2=P_{\mathrm{RIS}},\ 0<A_{p,l}<1,\end{aligned}\tag{2.19}$$

where $F\left(r_{1,h}\right)$ and $H\left(r_{1,h}\right)$ depend only on $r_{1,h}$ and can be extracted from (2.15) and (2.13), respectively. We now define

$$\begin{aligned}\Lambda\left(r_{1,h},\mathbf{A},\mu\right)=&\ F\left(r_{1,h}\right)\left(\sum_{p=1}^{M_x}\sum_{l=1}^{M_y}A_{p,l}\right)^2\\&-\mu\left(H\left(r_{1,h}\right)\sum_{p=1}^{M_x}\sum_{l=1}^{M_y}A_{p,l}^2-P_{\mathrm{RIS}}\right),\end{aligned}\tag{2.20}$$

where μ is the Lagrange multiplier. By taking the first derivative of $\Lambda\left(r_{1,h},\mathbf{A},\mu\right)$ with respect to each $A_{p,l}$ and equating it to zero, it holds that $A_{p,l}$ should be equal for each other, given by (2.17) by replacing $r_{1,h}^*$ with $r_{1,h}$. Subsequently, by plugging $A_{p,l}$ into the objective function of (2.19), (2.18) is obtained from which $r_{1,h}^*$ can be obtained by a linear search.

Chapter 3

AI-Assisted MAC for Reconfigurable Intelligent Surface-Aided Wireless Networks: Challenges and Opportunities

3.1 Introduction

With the ever-increasing demands on wireless networks, research in wireless communications continues to focus on meeting the challenges of improving the energy efficiency (EE) versus spectral efficiency (SE) trade-offs. Advances in meta-materials have fuelled research in reconfigurable intelligent surfaces (RISs) for beneficially reconfiguring the wireless communication environment with the aid of a large array of low-cost reconfigurable elements. This new design paradigm results in migration from traditional wireless connections to “intelligent-and-reconfigurable connections". The intelligently controlled features of RISs lead to potential benefits for future wireless networks, such as their coverage enhancement, EE/SE performance improvement, leading to improved throughput and security [43]. Because of these potential benefits, RISs are eminently suitable for addressing various challenges of wireless communications; hence they have been extensively investigated in diverse applications. Although the benefits of RISs in the physical layer have already been validated in practice, their performance is still constrained by the medium access control (MAC) layer, since the real-time configuration of RISs is complex and hence costly. To address this problem and improve the benefits of RISs, artificial intelligence (AI)-based methods can be applied to design MAC protocols for RIS-aided wireless networks.

Most of the existing research activities on RISs focus on physical layer issues, such as the issues of RIS deployment and their sustainable operation, flexible beamforming reconfiguration, EE/SE performance improvement and their compatibility with emerging technologies such as non-orthogonal multiple access (NOMA), as well as massive multiple-input multiple-output (MIMO) aided millimeter-wave (mmWave)/terahertz (THz) communications [44]. Following the recent breakthrough in the fabrication of programmable metamaterials, RISs have been employed in various wireless networks. Some of the MAC-related issues have also been investigated in order to support seamless connectivity [45–55]. However, these explorations of the MAC layer have focused

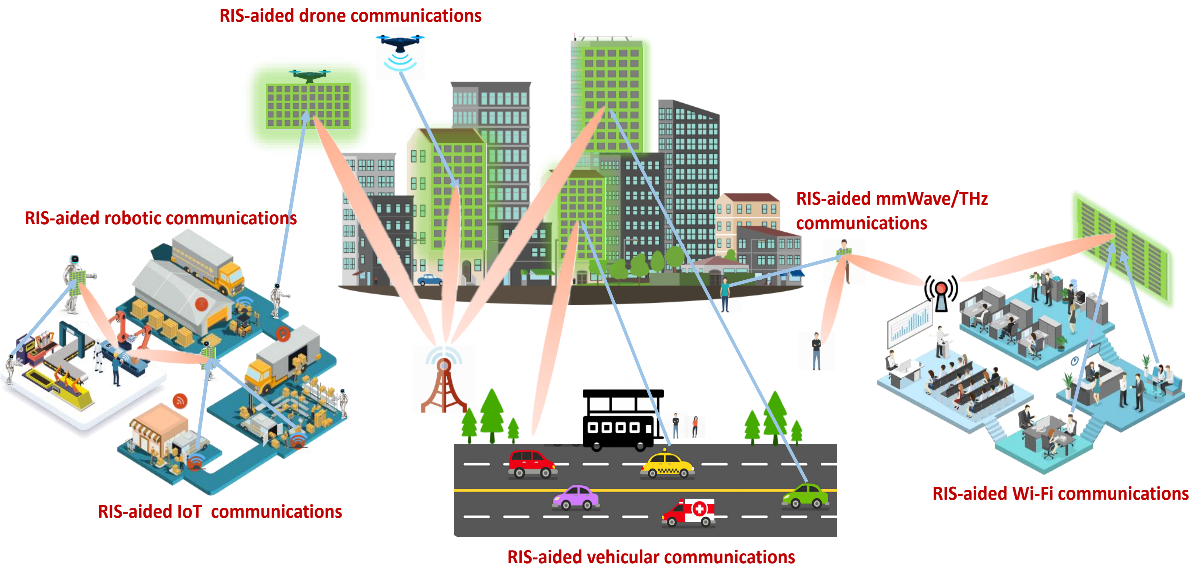

Figure 3.1: RIS-aided wireless network applications in multi-user communication systems.

primarily on the single-user uplink (UL) or multi-user downlink (DL). But there is a paucity of promising multi-user uplink solutions, since this scenario has not attracted significant attention to date. With the continued development of RIS technology and its integration with AI, the latency-sensitive services/applications supported by RISs are of salient importance in the 6G area, including RIS-aided vehicular, drone, or robotic communications, as shown in Fig. 3.1. Moreover, handling the massive number of RIS-aided sensors or Internet-of-things (IoT) devices represents a significant challenge in terms of the EE/SE. Finally, RISs are eminently suitable for supporting the emerging mmWave/sub-THz/THz communications in pursuit of high quality of service (QoS). Clearly, compelling MAC designs have to be conceived for fully exploiting the potential of RIS-aided wireless networks.

Against this background, we first present four typical scenarios (**S**) of RIS-aided multi-user wireless communications, with special emphasis on their MAC protocol design. Then, we propose three types of AI-assisted MAC structures designed for the RIS-aided multi-user uplink and discuss their protocols and applications. Next, we discuss some potential challenges facing AI-assisted MAC protocols. Furthermore, we evaluate the proposed AI-assisted MAC solutions to quantify their system throughput. Finally, we conclude with the trends in designing AI-assisted MAC protocols for RIS-aided wireless networks.

3.2 Scenarios, Protocols and Objectives

In this section, we commence by presenting our typical MAC scenarios seen in Fig. 3.2 and then review the existing MAC protocols and their design objectives.

3.2.1 Scenarios

- **S1: Single RIS-aided multiple-Tx single-Rx**. In S1, a single RIS is deployed to coordinate the uplink transmissions of multiple transmitters (Txs) to a base

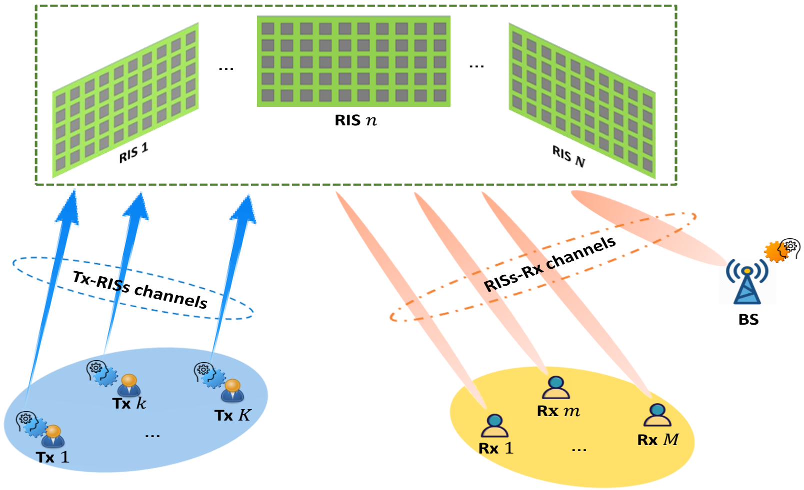

Figure 3.2: AI-assisted MAC scenarios in RIS-aided wireless communications.

station (BS), e.g., K Txs to a BS via an RIS. Note that the single-input single-output scenario is a special case when $K = 1$.

- **S2: Single RIS-aided multiple-Tx multiple-Rx**. In S2, a single RIS is deployed to coordinate the uplink transmissions of multiple Txs to multiple receivers (Rxs), e.g., K Txs to M Rxs via an RIS.
- **S3: Multiple RIS-aided multiple-Tx single-Rx**. In S3, multiple RISs are coordinated to support the uplink transmissions of multiple Txs to a BS, e.g., K Txs to a BS via N RISs.
- **S4: Multiple RIS-aided multiple-Tx multiple-Rx**. In S4, multiple RISs are coordinated to assist the uplink transmissions of multiple Txs to multiple Rxs, e.g., K Txs to M Rxs via N RISs.

For future networks with the ultra dense deployment of users, the coordination of massive users for meeting their QoS demands in the scenarios with a single RIS (e.g., S1 and S2) becomes challenging. For the scenarios having multiple RISs (e.g., S3 and S4), the user-RIS association (also known as RIS allocation) becomes more attractive, since serious interference may occur among the RISs.

3.2.2 MAC Protocols

Conceiving MAC protocols (**P**) for RIS-aided multi-user wireless communications have become essential. Both the conventional orthogonal multiple access (OMA) and the emerging NOMA schemes have already been investigated [45–55].

RIS-aided OMA. It aims for improving the SE/EE, for enhancing the QoS and for increasing the number of network connections by reconfiguring the wireless propagation environment[45–52]. The available OMA technologies integrated with RISs are enumerated as follows.

- **P1: RIS-aided time division multiple access (TDMA)**. It enables multiple users to transmit their data via RISs on the same frequency in different time slots [47–52].

- **P2: RIS-aided frequency division multiple access (FDMA)**. It enables multiple users to transmit their information via RISs in the same time slot on non-overlapping domain frequency channels [45, 46, 51].

- **P3: RIS-aided spatial division multiple access (SDMA)**. It enables multiple users to transmit their data via RISs either in unique angular direction or by exploiting the users' unique channel impulse responses (CIRs) by spatial multiplexing [53].

- **P4: RIS-aided carrier sensing multiple access (CSMA)**. It enables multiple users to transmit their signals via RISs relying on random contention-based multiple access protocols, where some control information exchange is required before the RIS-aided payload transmission [44, 55].

RIS-aided NOMA. With the assistance of RISs, NOMA schemes are capable of avoiding having to distinguish multiple users on the same resource block by their power levels, which may improve their SE/EE and latency. Hence, NOMA-assisted RIS-aided multi-user downlink communications have been explored in [53, 54], concluding that the performance of NOMA is not always preferable compared to OMA. For example, NOMA may perform worse than angularly-orthogonal SDMA or TDMA.

3.2.3 Objectives

The objectives (**O**) of MAC designs conceived for RIS-aided multi-user systems include the following potential aspects.

- **O1: System throughput**. The throughput is directly linked to the SE, which can be increased by increasing the number of transceivers and/or the time/ frequency/ space/ RISs resources.

- **O2: EE performance**. The EE is given by the capacity normalized by the MAC's energy consumption, which can be readily improved by the directional communications of RISs, which is mitigating the interference by directional beams and/or enhancing the strength of the desired signal reflected by passive elements. From a specific MAC design perspective, the EE can be further improved by avoiding access collisions. Therefore, a critical aspect of EE in the MAC is that of exploiting the angular focusing capabilities of RISs for multiple users.

- **O3: Fairness**. The rate fairness of different users should be guaranteed without degrading the overall system performance, especially when the resources are limited. In this context, avoiding these starvations of users suffering from low link quality becomes a pivotal criterion when designing an appropriate MAC for RIS-aided wireless networks.

- **O4: Overhead**. The overhead of user access-grant directly affects both the communication and computational complexity in terms of the RIS channel estimation, reconfiguration and resource allocation. Additionally, the wireless handshake of the MAC design may impose extra costs. How to implement the MAC protocol at a low-cost in RIS-aided wireless networks is a challenging dilemma.

- **O5: Latency**. The MAC design needs to meet the low-latency requirement of delay-sensitive applications with the aid of RISs.

Table 3.1: RIS-AIDED TRANSMISSION PROTOCOL DESIGN: STATE OF THE ART

Refs.	Scenar	Protocol	Objecti	Approaches	Applicatio	Key features
Centralized						
[45]	**S1**	**P1**, **P2**	**O1**, **O2**	Iterative algorithm	IoT	An RIS-aided transmission protocol with the RIS group partition for long distance transmission.
[46]	**S1**	**P1**, **P2**	**O1**	SDR, STM	mmWave, IoT	An RIS-aided transmission protocol with frequency-selective channels for delay-sensitive applications.
[47]	**S1**	**P1**	**O1**	Iterative algorithm	Wi-Fi	A pilot-assisted block transmission protocol for RIS channel estimation and passive beamforming with discrete phase-shift.
[48]	**S1**, **S3**	**P1**	**O4**	Iterative algorithm, supervised learning	RF sensing	A periodic configuring protocol aims to perform RIS-aided human posture.
[50]	**S1**	**P1**	**O5**	Iterative algorithm (BCD)	Edge computing	RIS aided TDD transmission is investigated in mobile edge computing systems.
[49]	**S1**	**P1**	**O1**	Iterative algorithm (SCA)	Drone communications	Jointly optimizing UAV trajectory and RIS beamforming for RIS-aided UAV communications.
[51]	**S3**	**P1**, **P2**	**O1**, **O2**	Iterative algorithm	IoT, massive	RIS-aided transmission combined TDD with OFDMA is discussed by jointly considering the user scheduling and power control.
[52]	**S1**	**P1**	**O1**, **O2**	Alternating optimization (BCD)	Wi-Fi	RIS-aided TDD transmission with considering perfect channel state information (CSI) and imperfect CSI.
[53]	**S3**	**P3**, **NOMA**	**O1**	Cauchy-Schwarz inequality	Edge computing	RIS-aided NOMA transmissions are used to serve multiple users on each orthogonal spatial direction.
[54]	**S1**	**NOMA**	**O1**, **O2**	Iterative algorithm (BCD, SDR)	Massive, low-latency	An RIS-aided NOMA with combined-channel-strength is proposed while ensuring the fairness among users.
Distributed						
[43, 44]	**S1**-**S4**	f×	**O1**-**O3**	f×	Wi-Fi, D2D, mmWave, IoT	Randomly access with information exchange in RIS-aided multi-user system.
[55]	**S1**, **S2**	**P1**, **P2**, **P4**	**O1**	Alternating optimization	IoT, D2D, Wi-Fi	Randomly reserved access in RIS-aided multi-user system.

Existing contributions on the MAC design of RIS-aided communication systems are summarized at a glance in Table 3.1, with an emphasis on their design objectives and critical features. In the table, the acronyms SDR, STM, SCA, and BCD represent semidefinite relaxation, strongest tap maximization, successive convex approximation and block coordinate descent, respectively. Notably, with the context of the coming wireless intelligence era, AI will give impetus to the MAC designs in RIS-aided networks by enabling the users and BS to “think-and-decide".

3.3 AI-Assisted MAC for RIS-Aided Networks

In this section, we design three AI-assisted MAC architectures for RIS-aided wireless networks, namely for centralized, distributed and hybrid schemes. We discuss their differences from the perspective of their overall framework, protocol design, computational aspects and promising applications. In particular, the centralized and hybrid MAC protocols are time-frame based, while the distributed MAC protocol is based on a random access scheme. The centralized MAC design obeys a central schedule, the distributed MAC design uses a contention-based model, and the hybrid MAC design combines both features. Additionally, deep learning and reinforcement learning solutions are adapted to the different MAC protocols.

3.3.1 Centralized AI-Assisted MAC

Framework

In the proposed centralized AI-assisted MAC framework, the BS tightly coordinates the multiple access of users. Explicitly, the BS enables each of the RIS-controllers to beneficially configure the wireless propagation environment via deep learning for multiple users. Here, the RISs are assumed to be passive, simply reflecting the incident signals without sensing or processing. More explicitly, the BS has to estimate the concatenated BS-RIS-user link, calculate the RIS phase reconfiguration, and allocate resources via deep learning, as it will be detailed below in the ‘computation’ part. As shown in Fig. 3.3, each sub-frame is divided into three periods: the pilot period, computing period and scheduled transmission period. The pilot period and scheduled transmission period can be further divided into K pilot slots and J data slots, respectively. The users transmit their data in the J data slots over the N non-overlapping sub-channels. Based on this, the centralized AI-assisted MAC protocol is designed by giving full cognizance to both channel estimation as well as phase computation and data transmission.

Protocol

The protocol of the centralized AI-assisted MAC is shown in Fig. 3.3, which is integrated with TDMA and FDMA, where each user obeys the time division scheme in each sub-channel. In particular, after synchronization, each user initiates pilot transmission to the BS in dedicated pilot slots. During the computational period, the BS first estimates the concatenated RIS link, followed by time, frequency and power resources allocation and RIS phase configuration. Then the BS instructs each RIS-controller to configure its reflection parameters and schedules the access of users, who transmit their data to the BS via the RISs.

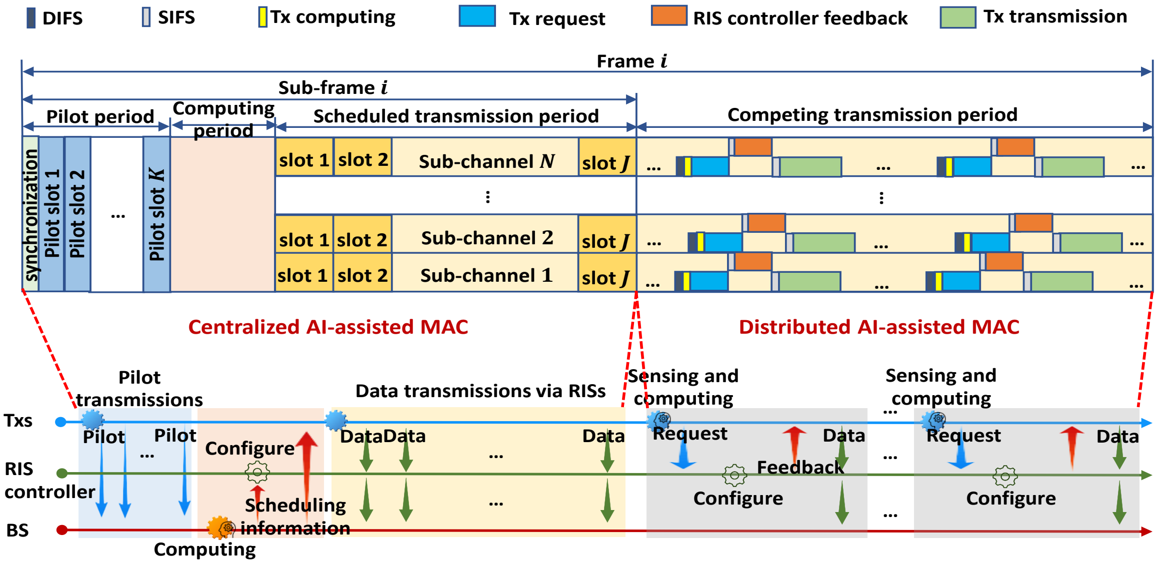

Figure 3.3: Hybrid AI-assisted MAC structure with centralized and distributed designs, an illustration of Case 1.

Computation

Given the excessive complexity of high-dimensional full-search-based centralized MAC protocols, a deep learning-based computational model trained offline can be employed at the BS for finding a near-optimal solution at a reduced complexity. The input of the trained deep learning model can be the number of users, the number of sub-frames, the number of channels, the number of RISs and the RIS channel information. The online inference that moves the complexity to offline training is performed at the BS, which relies on a model-based training for determining the RIS phase-shift configuration, the RIS-deployment strategy and the resource allocation strategy, which are related to each other. More explicitly, these related learning tasks share the same input parameters, thus learning multiple related tasks jointly improves the prediction accuracy and generalization capability compared to learning them separately.

Applications

Given the centralized implementation and deep learning-based computation model considered, the centralized AI-assisted MAC design advocated can be readily applied to the scenarios S1 and S3 for supporting low-power RIS-aided communications.

3.3.2 Distributed AI-Assisted MAC

Framework

In contrast to the centralized scheme, in the proposed distributed AI-assisted MAC framework, each user configures the multiple access and computes the RIS configuration by itself based on the RIS-aided network environment. In this case, no BS assistance is necessary. Each RIS is assumed to be passive and to occupy a non-overlapping frequency channel. In contrast to the centralized MAC design, the user has to negotiate with the RIS-controller for channel access. The corresponding RIS-aided data transmission as illustrated in Fig. 3.3. In particular, channel sensing and computation are carried out at the user side via reinforcement learning (RL) to determine the RIS configuration. Once a channel is idle, the user sends the RIS configuration information to the RIS-controller to negotiate the ensuing RIS-aided data transmission.

Protocol

The protocol of the proposed distributed AI-assisted MAC is shown in Fig. 3.3, which is integrated with CSMA and FDMA, where each user follows the distributed coordination function (DCF) based scheme in each channel. In particular, a competing user senses the state of each sub-channel. Once a channel is sensed to be idle, the user contends for the access to the channel. Waiting for a DCF inter-frame space (DISF) and backoff, the user computes its RIS configuration based on RL and sends an RIS configuration request to the RIS-controller. If the RIS is available for the user, the RIS-controller configures its reflection parameters and sends its feedback to the user after a short inter-frame spacing (SIFS). Following the elapse of a SIFS, the user then transmits the data to the BS via the RIS. Note that the feedback from the RIS-controller is sent without a transmit radio frequency chain. Moreover, the access collisions of users can be alleviated by the RIS-controller.

Computation

In the distributed MAC protocol, an RL-based computational model can be employed by each user to solve the resource allocation and RIS configuration problems because no RIS channel-information exchange is required. The RL model includes the following aspects: the current RIS configuration, the current RIS deployment, and the currently occupied resources (e.g., power) of each user. The model actions include three aspects: the update of RIS configuration, the motion-trajectory of the user and the occupied resources updates. The reward function is decided by the throughput requirement of the user. When the action taken by the user improves its data rate, the user obtains a positive reward. By contrast, for throughput reductions, the user receives a negative reward (also termed the penalty). The RL-based computational model is more suitable for small RISs to avoid potential dimensionality problems. If the RIS is large, the RIS elements may be partitioned into groups, where each group maintains the same RIS configuration.

Applications

Due to the distributed implementation and the RL-based computational model, the distributed AI-assisted MAC design can be applied to all the scenarios S1 to S4 for meeting low-latency requirements.

3.3.3 Hybrid AI-Assisted MAC

Based on the centralized and distributed MAC frameworks proposed, we now discuss three types of hybrid AI-assisted MAC designs, where the centralized and distributed implementations are integrated into a single frame.

Case 1

In this hybrid framework, the scheduled and the competing transmissions relying on RISs are combined after the pilot transmissions and computing, while enabling users to switch between them for meeting different QoS demands, as illustrated in Fig. 3.3. Each frame is partitioned into four parts, namely, the pilot period, the computing period, the scheduled transmission period and the competing transmission period. According to the proposed distributed AI-assisted MAC design, the scheduled users transmit their data to the BS via RISs in the scheduled transmission period. After that, based on the distributed AI-assisted MAC design, the unscheduled users (i.e., the unserviced users that have sent their pilots and the new requesting users) transmit their data to the BS or the Rxs via RISs during the competing transmission period. Given the dynamic switching between two transmission modes, this scheme is capable of maintaining the target-rate, and it may be suitable for all scenarios (i.e., S1 to S4).

Case 2

In this hybrid framework, the competing requests and the scheduled RIS-aided transmissions are combined into a single frame. Each frame consists of the competing request period, the computing period and the scheduled transmission period. The user sends a request to the BS and when a sub-channel becomes available during the competing request period, then the BS issues a feedback for acknowledgment. Based on the requests received, the BS controls the RISs and sends the scheduling information to users during the computing period. Afterwards, the scheduled users transmit their data to the BS via RISs in the scheduled transmission period. Due to the competitive access of Case 2, it can be applied in scenarios S1 and S3 for supporting RIS-aided smart homes or smart factories.

Case 3

This hybrid framework is similar to Case 2, since it combines the competing requests and the reserved RIS-aided transmissions into a single frame. The slight difference is that computing in Case 3 is carried out at the user, rather than at a BS or RIS-controller. When a sub-channel becomes idle, the user occupies the channel, then computes the required resources and RIS configuration based on RL and sends a request to the RIS-controller for reserving the resources for future RIS-aided transmissions. The RIS-controller sends a feedback to the user once a request is registered and controls the RIS. When the reserved transmission period arrives, the user transmits the data to the Rx or the BS via the RIS in the reserved slots. Since RL is mainly used for complexity reduction, Case 3 can be applied in all the scenarios S1 to S4 for supporting RIS-aided periodic communications.

In practice, due to the implementation constraints, the phase shifts applied by the RIS elements belong to a discrete set. Hence, the RIS configuration may be viewed as a classification problem, which can be tackled by using deep learning. If the phase shifts can be configured continuously, e.g., for varactor-based RIS designs, the optimal configuration of the phase shifts of the RIS can be regarded as a regression problem.

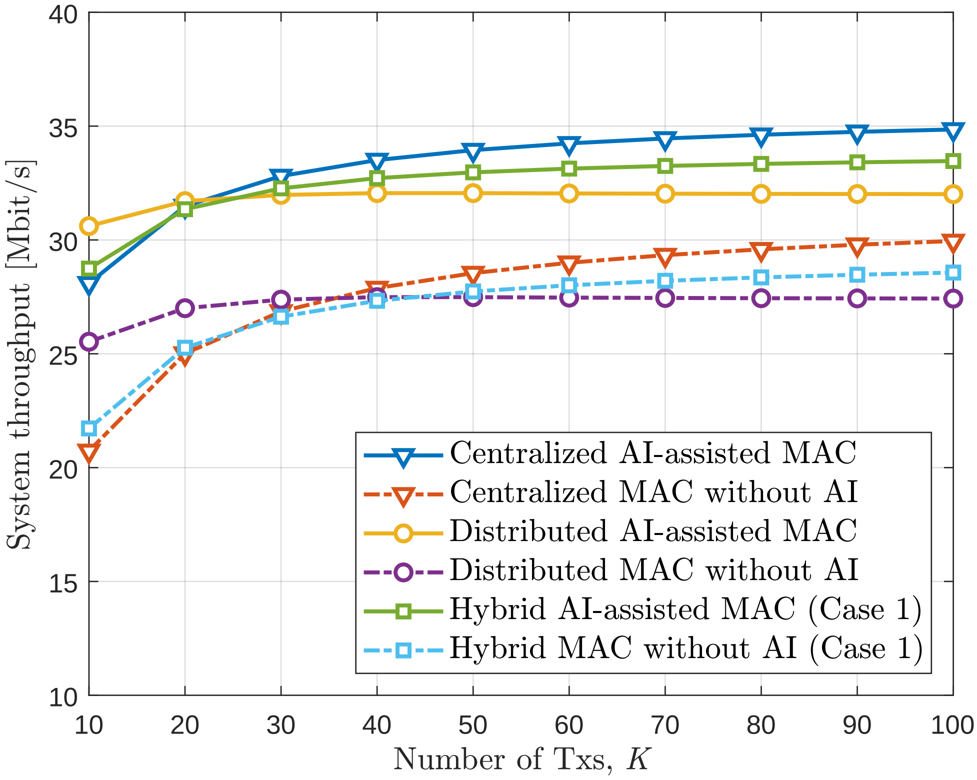

Figure 3.4: System throughput vs. the number of transmitters, where N=2.

3.4 Performance Evaluation

This section evaluates both the system throughput and the EE of the three AI-assisted MAC frameworks proposed for RIS-aided wireless networks. We opt for Case 1 as the hybrid MAC protocol. We consider a scenario that consists of a BS, 2 RISs having 128 RIS-elements each, and 100 single-antenna Txs, where the Tx-RIS and RIS-BS distances are 50 m and 30 m, respectively. A Rician fading channel model is assumed, where the Tx-RIS and RIS-BS channels benefit from the existence of LoS links having a path loss exponent of 2.2, while the Tx-BS channels are NLoS links with a path loss exponent of 3.6. The power dissipated at each user is 10 dBm, the noise power is -94 dBm, and the number of sub-channels is 2. Furthermore, we assume that each RIS occupies a single sub-channel as a benefit of interference cancellation, and each Tx is only allowed to use a single RIS to communicate with the Rx at a time.

3.4.1 System Throughput vs. the Number of Txs

Figure 3.4 shows the system throughput of RIS-aided wireless communications versus the number of Txs in the three types of AI-assisted MAC proposed. Firstly, it is observed that the system throughput of each AI-assisted MAC is improved compared to the MAC without AI, since AI methods have the potential of reducing the computing time. Observe from Fig. 3.4 that the throughput of each MAC initially increases, but then tends to saturate as the number of Txs increases. This is because the computation time ratio within each frame is reduced upon increasing the length of each frame. Also, the system throughput of the distributed MAC exhibits a slight lesion after saturation due to the competition collisions. Additionally, the system throughput of the distributed MAC is best when the number of Txs is low (e.g., less than 20). As the number of Txs increases, the system throughput of centralized MAC becomes higher than that of the distributed MAC and the system throughput of hybrid MAC (Case 1) is in the middle.

3.4.2 EE Performance vs. the Number of Txs

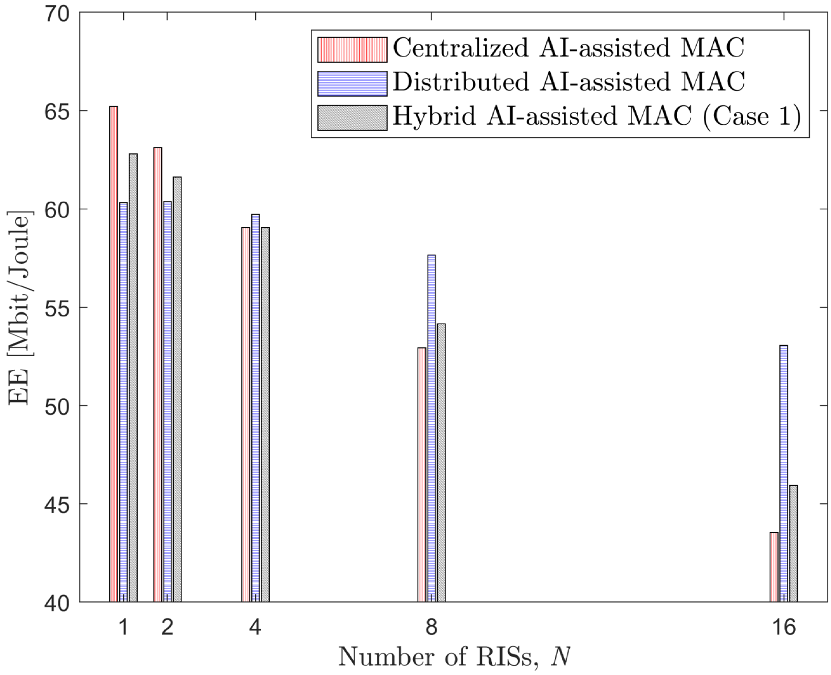

Figure 3.5: Energy efficiency vs. the number of RISs, where K=100.

Figure 3.5 shows the EE versus the number of RISs for all three types of AI-assisted MAC. It is observed that the EE of each type decreases as the number of RISs increases due to the increased computational complexity associated with extra computing time. Additionally, the EE of the centralized AI-assisted MAC is better than that of the distributed AI-assisted MAC, when the number of RISs is 1 or 2. As the number of RISs increases to 4, 8 or 16, the EE of the distributed AI-assisted MAC has the edge, because the overhead imposed by the centralized AI-assisted MAC is increased. In other words, the centralized AI-assisted MAC is suitable for a small number of RISs, while the distributed AI-assisted MAC is recommended for a large number of RISs.

3.5 Conclusion

In conclusion, we have presented four typical scenarios of RIS-aided multi-user communications. We then have reviewed the family of MAC solutions conceived for RIS-aided wireless networks and highlighted a range of competing MAC designs conceived for AI-assisted MAC structures relying on centralized, distributed and hybrid implementations. In particular, the centralized AI-assisted MAC excels in satisfying the target QoS of users, while the distributed AI-assisted MAC is more capable of meeting the random or unpredictable requirements of users. Finally, the family of hybrid AI-assisted MAC solutions strikes a beneficial trade-off between them. As performance evaluations revealed, distributed AI-assisted MAC schemes are more applicable to networks with small numbers of users associated with a large number of RISs. By contrast, the centralized AI-assisted MAC schemes are more suitable for a large number of users in conjunction with small numbers of RISs.

Chapter 4

Development of a System Level Simulation Model for D-band Networks

4.1 Introduction

This chapter describes the update of the system level simulation model for D-band networks in realistic environments, which was initially introduced in D4.2. Specifically, a square geographical area is simulated, where four rectangular obstacles are deployed. Moreover, we assume the presence of one mobile user and a specific number of access points which are placed in predefined coordinates inside the simulated area. Also, time evolution is incorporated in the simulations, as user's coordinates change over time according to a specific mobility model. In comparison with the initial setup of the system simulation model, this version is enhanced in several sections. The main differences concern user's mobility model and path loss modelling. Particularly, the trajectories of the user have extra degrees of randomness and therefore they have a greater diversity. Regarding path loss modelling, in this version a large scale fading term was added to the received power balance. This term forces user's received power to change into a stochastic quantity.

The main objective of the system level simulation procedure focuses on the production of data that will used by AI-based techniques for blockage forecasting, proactive handover and efficient resource allocation. The specific kinds of data that will be exploited for that purpose are the coordinates and velocity of the user for every time moment of a simulation session, as well as the received power of the user from every access point. In general, the parameters of the simulations can be adjusted in order to demonstrate several scenarios and use cases of interest. For example, we can adjust the dimensions of the simulated area and the number of users and access points, in order to correspond to an indoor environment (Scenario 2.1 – Deliverable 1.1), to an urban, suburban or rural environment etc. Moreover, simpler cases concerning the mobility of transmitters (Tx) and receivers (Rx), respectively, could be demonstrated. Such an example is the case of outdoor backhaul/fronthaul networks of fixed topology (Use Case 1 – Scenarios 1.1 and 1.2 – Deliverable 1.1). Finally, the most important contribution of this tool, will be the simulation of several schemes that will constitute the necessary inputs for the software demonstrator in the framework of WP5 (Task 5.4: Intelligent D-Band network demonstration).

4.2 System Level Simulation Model

The updated system level model which has been further developed to produce the sets of data which are used by the AI based techniques for blockage forecasting and proactive handover, is described as follows. Firstly, there is a geographical area, which is considered as a square with dimensions 50 $m\times$ 50 m. Secondly, there are four obstacles within this area, which are modelled as rectangular parallelepipeds with dimensions 9.5 m $\times$ 10 m $\times$ 5 m. They are located uniformly and symmetrically in the simulated area. Moreover, there are six access points, which are fixed in predefined coordinates. They are placed at height of 2 m from the ground. Also, we assume the presence of one mobile user, who is demonstrated by a point placed in the simulated area. Access points and users cannot be placed on the obstacles. In order to involve time evolution, it is assumed that a simulation session has duration T. Each session is divided in successive time slots. Each of them has duration dt. For the mobility of the user, we exploit the following model. At first, user's initial place is chosen randomly within the simulated area. Then, user tries to reach a random destination point. The destination point changes randomly every $\frac{T}{3}$, in order to achieve diversity of user's trajectories. This is a significantly different mobility model compared with the one that was deployed in the previous version of the system level simulation model. Specifically, in D4.2/Chapter 4, user's destination was set at the beginning of each simulation session and did not change until the end. Therefore, the generated trajectories were simpler. Due to this fact, AI processing techniques were not so efficient. Also, the movement of a mobile user takes into account the obstacles of the environment. These affect the movement pattern of the users. Specifically, a user node has to change its trajectory when encounters an obstacle [56]. Furthermore, velocity V of a user is constant during a specific time slot. Its value is a random variable, which is uniformly distributed over the interval $[0, V_{max}]$. V_{max} is the maximum allowable value of user's velocity. Thus, the displacement dS of a user during a time slot is: $dS = V \times dt$. The direction of dS is determined by the relevant mobility model. Such examples are depicted in Fig. 4.1 and Fig. 4.2, respectively. Specifically, the top view of the simulation area is depicted and user's trajectory is represented by successive dots of specific colour. The biggest dot corresponds to the first time slot of the simulation, while the smallest one corresponds to the last time slot. The corresponding simulation parameters, as well as the coordinates of the access points (purple dots), which are the same for both cases, are shown in 4.1 and 4.2, respectively.

Finally, each mobile user is allocated to the nearest LOS access point during the first time slot of the simulation and remains allocated to the same access point until the end of the simulation, independently of the condition of the link between user and serving access point (LOS or not) during the next time slots. We have to mention that the policy regarding the allocation of a user to a specific access point, the number and coordinates of the access points as well as simulation parameters can be modified depending on the scope of the simulation scenarios.

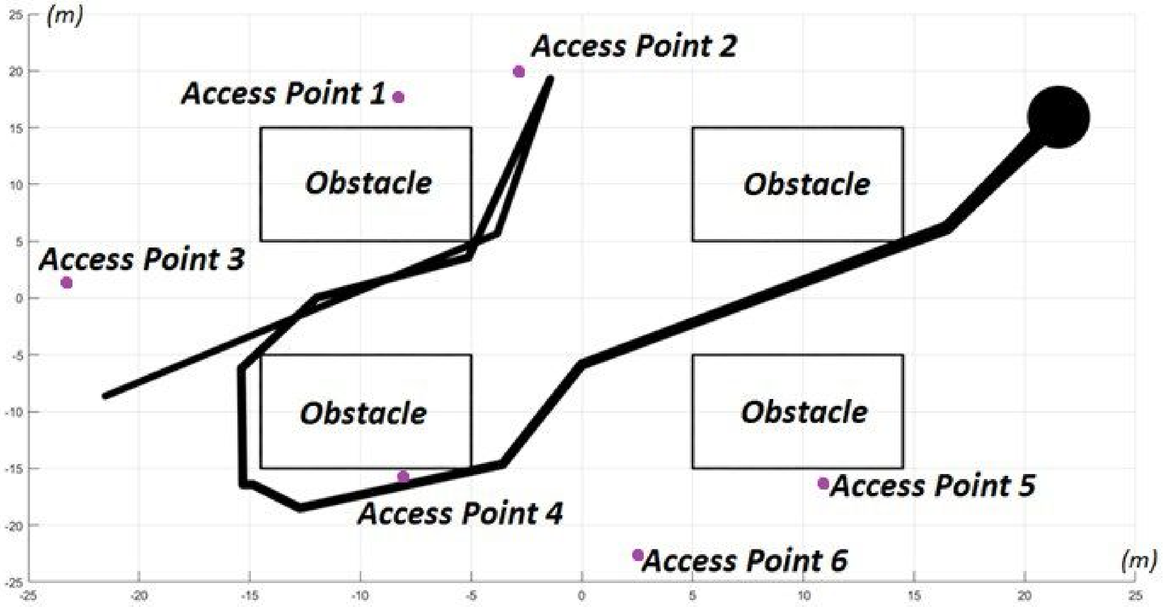

Figure 4.1: Indicative simulation example for six access points and one user (a).

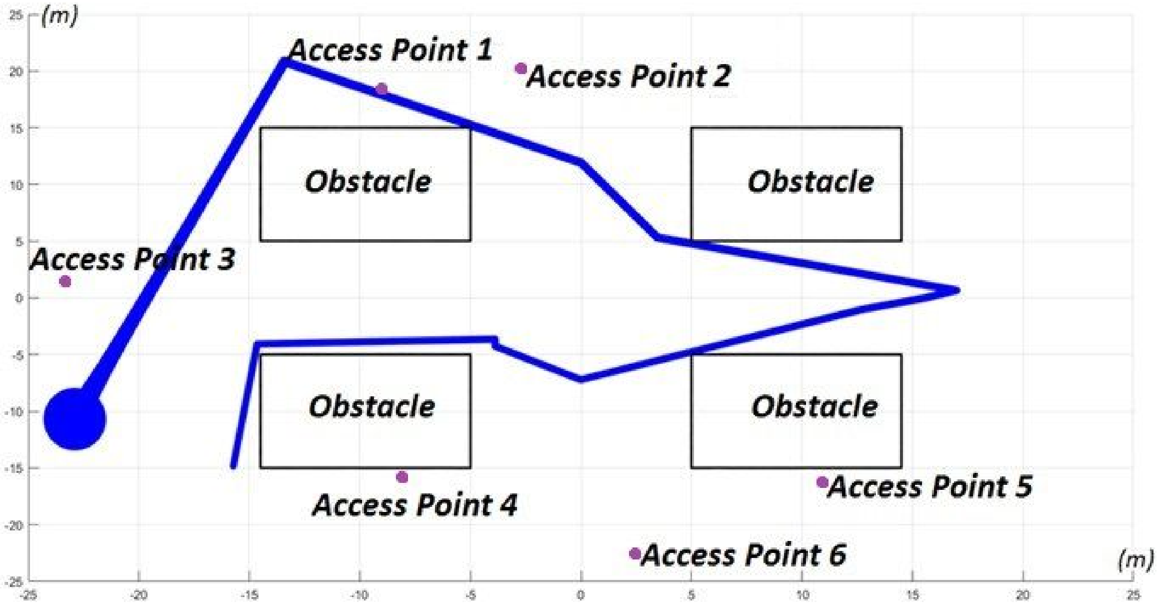

Figure 4.2: Indicative simulation example for six access points and one user (b).

Table 4.1: Simulation parameters for Fig.1 and Fig.2

$T(sec)$	300
$dt(sec)$	0.05
$V_{max}(m/sec)$	16

Table 4.2: Coordinates of access points

	$x(m)$	$y(m)$
Access Point 1	-8.37	17.65
Access Point 2	-2.88	20.22
Access Point 3	23.34	1.62
Access Point 4	10.82	-16.03
Access Point 5	-8.17	-15.61
Access Point 6	2.43	-22.56

4.3 Path Loss Modeling

In order to map the received power of a user from every access point at a specific time slot, we make use of Friis's equation [57],[58]:

$$P_R = P_T + G_T + G_R + 20log\frac{\lambda}{4\pi \times d_0} - 10n \times log\frac{d}{d_0} - \chi_\sigma \tag{4.1}$$

where P_R is the received power (in dBm), P_T is the transmitted power (in dBm), G_T and G_R are the gains of the Tx and Rx antennas, respectively (in dBi), λ is the free space wavelength (in m), n is the Path Loss Exponent (PLE), d_0 is the reference distance (in m – usually $d_0 = 1m$), d is the distance between Tx and Rx (in m) and χ_σ is the large-scale fading (a zero mean Gaussian random variable with a standard deviation in dB).

We have to mention that the difference between the above Path Loss model and the one that was deployed in D4.2/Chapter 4 is the incorporation of the large-scale fading term χ_σ. Specifically, χ_σ is a term which modifies user's received power from a deterministic quantity to a stochastic one. This is something that makes simulations more realistic. The PLE values and the respective standard deviation of large-scale fading in an urban microcell or a small-cell environment, where carrier frequency is considered as $f = 142\ GHz$, are set as follows [58]:

- $n = 2.1$ and $\sigma = 2.84$ dB for LOS links (non blocked channel
- $n = 3.1$ and $\sigma = 8.25$ dB for Non-LOS links (partially blocked channel)
- or $n = 3.6$ and $\sigma = 9.10$ dB for Non-LOS links (partially blocked channel).

If the wireless channel between a user and an access point is totally blocked, the received power of a user is considered to be equal to the default noise level. A detailed classification of the states of the wireless channels (i.e. non blocked, partially blocked or totally blocked channels), is described in detail in D4.2/Chapter 4.

4.4 Mapping of Received Power

Two typical examples of the power that user receives from every access point as function of time is mapped in Fig. 4.3 and Fig.4.4, respectively. Specifically, 4.3. corresponds to the case of Fig.4.1 simulation session, while Fig.4.4 corresponds to the case of Fig.4.2 simulation session. In both scenarios, we assume that carrier frequency is f = 142 GHz as it is mentioned previously, the transmitted power is P_T = -7 dBm, the gains of the user and the access points antennas are G_T = G_R = 12 dBi and the default noise level is -128 dBm. Regarding Fig. 4.3 and Fig.4.4, we have to note the following. When the link between user and access point is not totally blocked, the value of user's received power, is mainly determined by the distance between them and the value of PLE in each case, according to channel state (non blocked or partially blocked). Actually, large-scale fading term causes an oscillation of the received power around this deterministic value. Moreover, we can observe that there are long time intervals during a simulation session where the wireless link between each access point and user is LOS or totally blocked. On the other hand, the partially blocked state of the wireless channel, lasts significantly less time. Also, there is a great number of transitions from a LOS link to a totally blocked link and vice versa, between user and access points. This results from the randomness of the shape and the length of user's trajectory within simulated area. Finally, it is mentioned that in Fig. 4.3, there is one time interval during the first time slots of the simulation session where all of the access points are totally blocked to the user, while in Fig.4.4, Access Point 4 and Access Point 5 are always totally blocked. In all of these cases, the received power from the corresponding access points, is constantly equal to the default noise level (-128 dBm).

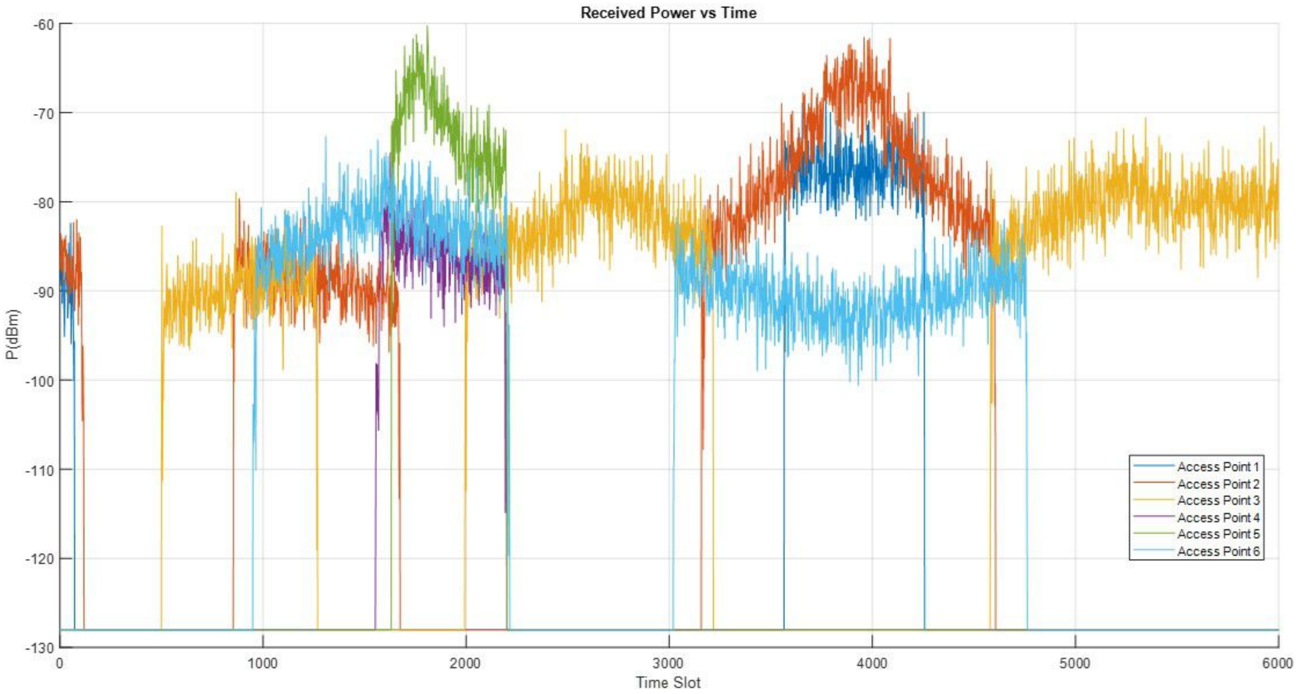

Figure 4.3: Received Power vs Time for user of Fig.1.

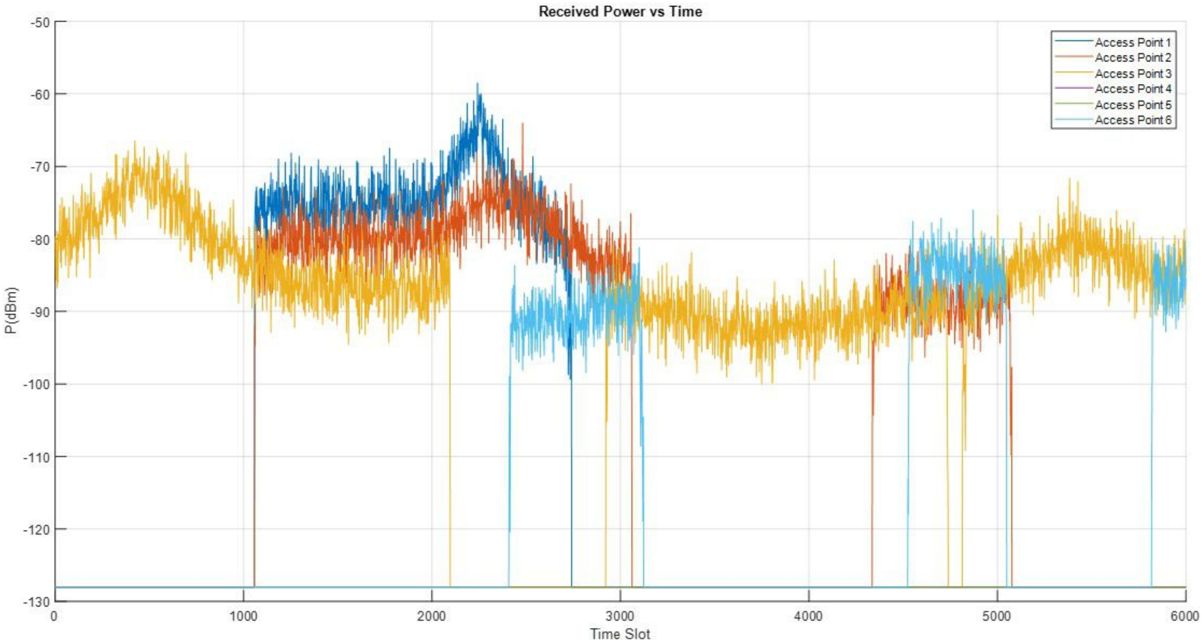

Figure 4.4: Received Power vs Time for user of Fig.2.

4.5 Conclusion

In this chapter, an updated system level simulation model for D-band networks was presented. Specifically, within the simulated geographical area, we assume the presence of four rectangular obstacles, a number of access points which are randomly placed and one mobile user. The main differences compared with the previous version of this simulation model focus on a user's mobility model and path loss modeling. Specifically, user's trajectories are now more random and complex. Hence, they have a greater diversity. Regarding the path loss model, in this version a stochastic term which corresponds to the large scale fading, was added to the received power balance. These additions could be exploited by AI based techniques, in order to become more efficient in the forecast of forthcoming blockage effects.

Chapter 5

AI/ML Applications for Line-of-Sight Aware Connectivity

5.1 Introduction

In the era of wireless communication, the heterogeneous nature enabling numerous access networks, frequency bands and cells together with overlapping coverage areas poses various network design and implementation related issues for wireless networks. Even though, the use of machine learning and artificial intelligence in wireless communication networks is still in its development phase, it will expand over time to create smarter and reliable networks with an expansion of Internet of Things (IoT) devices. Machine learning (ML) and artificial intelligence (AI) play a crucial role in deploying, operating, and managing 5G networks. ML and AI may be applied to a variety of use cases to assist wireless networks in transitioning from a human-driven management paradigm to self-driven autonomous management, thereby revolutionizing network operations and maintenance processes. However, in order to achieve reduced network latencies, enabling event-driven analysis and a real-time processing, a paradigm shift from today's centralized and virtualized cloud-based AI to a distributed AI architecture with decision-making intelligence will be required. The availability of high-performing and efficient computing resources is one of the primary facilitators of a sustainable AI integration. Indeed, 5G systems aim to provide high throughput and ultra-low latency communication services. Moreover, machine learning enables to discover various patterns in large datasets for data enrichment to make better predictions and decisions about where and how to deploy resources to avoid demand crunches and system failures.[59][60][61]

The layout of this chapter is as follows. Firstly, we present an initial analysis of the challenges and opportunities for machine learning in the channel modeling domain for both line of sight (LOS) and non-line of sight (NLOS) scenarios. The objective here is to understand the feasibility of predicting LOS connectivity at the physical layer. Secondly, extended version of channel modeling prediction and to analyze statistical relation between condensed parameters of multi-dimensional mobile channels and geometrical link condition, which is an ongoing work together with our partner Aalto university. Last but not the least,we will share analysis and results on the application of ML to predict LOS blockages, instead of just identifying them using computationally expensive blockage identification methods. These predictions can act as input to quickly construct the feature-set, required by the “assignment and blockage minimization” predictor. This hierarchical use of predictors is another direction of our work that holds the potential to simplify and speed up connectivity establishment in real-time. We conclude by hinting on potential future extension of presented works, such as expanding the scope of problem definitions to a dynamic network where user equipment (UE) to access point (AP) assignments and predicting LOS connectivity are more challenging.

5.1.1 Problem Definition

The problem landscape in ARIADNE includes various connectivity scenarios, that have been structured under various use cases in the deliverable report D-1.1. These include indoor, outdoor environments, where LOS and NLOS links need to be established. Such scenarios can be addressed at different network layers individually or jointly. At the physical layer, it may be of interest to predicting signal strength, directionality and existence of LOS connectivity of the multi-path channels based on the propagation environment. At the link level, the connectivity scenarios may take into account the topological properties of the network, such as the AP and UE densities that reflect the habitation, structural or ad hoc aspects of the network or its environment. The objective here is to tap the potential of these upcoming network entities to break the limitations imposed by LOS links, thereby increasing the number of feasible UE-to-AP assignments beyond what is possible to-date. However, Formulating an AI/ML problem is sometimes not obvious from the start and requires analysis, and data level understanding, which is often divided among multiple people, who need to collaborate in a structured and targeted manner. The established procedure to organize such interactions is “Cross-Industry Standard Process for Data Mining” (CRISP-DM) [62] and this is indeed the methodology that has been used in ARIADNE. CRISP-DM approach has helped to build domain-level and data-level understanding, framing and solving the data mining (AI/ML) problems and iterating over solutions. With this methodological background clarified, we now proceed to present our framework, and subsequently the results from applying it to the directional LOS connectivity use case.

5.2 ML Model for Environment-Specific LOS Connectivity

Starting with the preliminary stage, data was collected from various routes where the UE moves. The transmitter (Tx) and receiver (Rx) information from the different locations(between the start and end location of the route of the moving UE) were interpolated and fed into the machine learning model, along with the channel attributes of Multipaths, including complex amplitude, delay, departure angle (AAoD), departure angle(EAoD), arrival angle (AAoA), arrival angle (EAoA), Delay spread angle (DSA), Azimuth angle (AA). After pre-processing the data, the statistical characteristics of the channel(including expectations and the extension of these parameters) were obtained to train ML algorithms. One of the main challenges at the physical layer is to predict the properties of the channel on the receiver side. Since the current available datasets had a limited feature set and observed error margins such as the root mean square errors (RMSEs), our approach relies on investigating the existence of pattern within the available features as well as bringing geographic location as a first step to include environmental features to examine the density according to the user mobility for predicting LOS connectivity. Initial analysis reveals a certain degree of correlations among attributes when location information is included, but the predictive modeling aspects require further engineering of features for developing and deploying various KPI's focusing accuracy, fading statistics, correlations, complexity, and versatility which can find the hidden non-linear relationships among different features and can indeed improve the feasibility and viability of the model. In general, we aim to deliver more dynamic settings that changes over user mobility and can be incorporated in form of real time simulations. In particular, real world scenarios have moving users towards certain directions resulting in loss of connectivity approaching an object or wall. So the data generated will be used by AI based techniques to access the efficacy of LOS connectivity. Gradually this process will trigger a pro-active handover process in order to identify the patterns depending on user mobility on different routes under outdoor/indoor environment.

5.2.1 Explorative and Predictive Challenges

The problem with channel related predictions was further divided into two parts, where one part can focus on the behaviour of raw or fine granular form of individual path data and the second part can focus on aggregate (coarse granular) data subject to feature engineering. The former can be used to predict the presence of the LOS or NLOS path, pathloss for higher gain, or higher power, delay spread, etc. Determining LOS or NLOS is a major challenge in wireless communication, where we can bridge the gap with machine learning algorithms as the current literature has not extensively explored this area. The latter holds the promise to predict the link level behaviours e.g., for a given location, the properties of a link proportional to the received power. Previous investigations examined datasets with 2 routes and then 13 routes representing LOS and NLOS but were limited to extract patterns using machine learning algorithms. However, more/extended sites/routes would have helped to predict the coverage power more effectively. Real values from available data was classified to extrapolate the range of average values between two (start and end) locations of the users and observe other characteristics in this range of values. Moreover, with the information on start and end location coordinates of MS routes,intermediate MS location were derived by linear interpolation of the distance between the start and end locations. In order to understand the complex inter-relationships, commonalities or dissimilarities in data, the main objective was further extended by gradually linking the environment-related attributes like the user's location/position, density, etc.to be appended to data, to realize more generalized concept. This approach would hopefully help in understanding the relation of environmental traits and may also lead to a more comprehensive analysis. So for the potential future direction of this work, additional features from the ray tracing map, which acts as a blueprint of the original environment was measured considering channel data. Assuming that this may help to further refine the scope of the problem e.g., by examining the density or user mobility. Uncovering the influence of environmental characteristics, such as mobility or structural properties may also help shape the prediction problem. Additionally, a multi-path propagation approach would help in many scenarios such as how the link distance diffuses dispersion patterns for small scale

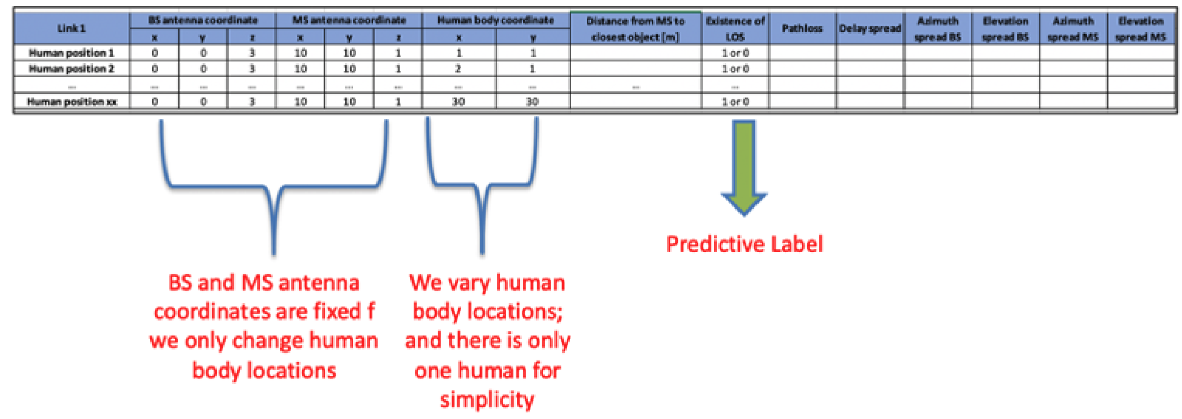

Link 1	BS antenna coordinate			MS antenna coordinate			Human body coordinate		Distance from MS to closest object [m]	Existence of LOS	Pathloss	Delay spread	Azimuth spread BS	Elevation spread BS	Azimuth spread MS	Elevation spread MS
	x	y	z	x	y	z	x	y								
Human position 1	0	0	3	10	10	1	1	1		1 or 0						
Human position 2	0	0	3	10	10	1	2	1		1 or 0						
...	...	...	...	...	...	...	...	...	...	...						
Human position xx	0	0	3	10	10	1	30	30		1 or 0						

BS and MS antenna coordinates are fixed f we only change human body locations

We vary human body locations; and there is only one human for simplicity

Predictive Label

Figure 5.1: Summary of LOS and NLOS routes dataset

and big scale problems with the angular distribution of the signal wave. Other micro- and macro-cellular scenarios and other parameters that are essential for evaluating the potential of two polarized MIMO systems are also the goals worth pursuing to see if they outperform the conventional methods.

5.2.2 Data Generation and Extraction

To extend the study for environment aware connectivity, the data was extracted from Helsinki-Vantaa airport Terminal 2 ray-tracing based on expert knowledge that allows to generate a specific network scenarios. Dataset includes 3,987,488 rows and 18 columns/feature where we simulate geographic location of 2 BS locations, 1412 MS location and 1412 human body locations. Table 1 shortly present the attributes/feature set of the datasets. The structure of files are seen in Table 5.1 and Figure 5.1

Table 5.1: Dataset extracted from Helsinki-Vantaa airport Terminal 2 ray-tracing

Attributes	Description
BS index	2 locations
MS index	1412 locations
BS location [x y z]	[x y z] co-ordinates
MS location	[x y z] co-ordinates
Human body location	[x y] co-ordinates
Distance to closest object	[m] meters
Distance to walls 1, 2, 3, and 4	[m] meters
LOS condition	(1 = yes, 0 = no)
Path loss	[dB] Decible
Delay spread	[ns] Nano seconds
BS azimuth angular spread	[deg] Degree
BS azimuth elevation spread	[deg] Degree
MS azimuth angular spread	[deg] Degree
MS azimuth elevation spread	[deg] Degree

5.3 AI-Constrained Optimization for Adaptive UE-AP Association

Another central problem which has been addressed in WP4 is the allocation of resources i.e. optimally associating each UE to an AP which can satisfy resources required by the UE and with whom, the partial LoS blockers are completely avoided or minimized. This problem along with its system model, data generation and a hybrid AI/ML based solution has been contributed in the previous deliverables (chapter 4 of D4.1 and chapter 7 of D4.2). Further extension of this important problem is work in progress, where the aim is to address some of the more challenging but also more realistic aspects in terms of resolving the UE-AP association problem in an evolving network. Thus, the association problem in this next phase, transforms into a recurring problem to be solved on a continuous basis, because the network is always evolving and hence the AI/ML needs to deliver an adaptive solution in real time.

To enscope the recurring UE-AP association problem and evaluate the AI/ML solutions, additional concepts need to be defined that allow to emulate an evolving or changing network. The solution can then be evaluated for its quality and algorithmic performance. First, the concept of triggers is being addressed. A trigger in this context is an event that changes the state of the network in terms of its system model. A non exhaustive list of triggers have been identified as follows:

- Addition or removal of a UE
- Removal of an AP
- Movement of a UE

As a result of any of the above triggers, the state of network model changes, which requires the AI solution, for instance, the optimization to adapt as fast as possible by the underlying hardware. Adaptation means to recover the current best solution, which now represents outdated and infeasible associations. The quality of the next best solution (UE-AP assignment plan) naturally depends on how much time the solver is granted before the next best solution is retrieved. Hence, online optimization techniques can be employed to continuously monitor for the trigger events, update the network system model in the working memory of solver and remain in the active solving phase.

To emulate a changing network based on user controlled triggers, a GUI framework design is being conceived. Considering the nature of stated triggers, the optimization constraints (as defined in Deliverable D4.1 chapter 4) can be solved in a two-staged implementation process. First, the resource allocation constraint can be satisfied and in the next stage, the minimization of partial LoS blockages can be added because of the computational and integration complexity of the latter constraint.

Relation with ML model: The ML model that predicts the UE-AP association is based on training data that is generated from the best solution as found by the optimizer. In the case of adaptive UE-AP association, where the network undergoes changes and continuous optimization is employed, multiple snapshots of the best solutions can be stored. These can then be converted to training datasets (refer to Deliverable D4.1, chapter 4 for details). Hence, the ML model can be regularly retrained and updated in the background, which increases the intelligence of the model to be able to deal with different network situations and still deliver a reliable and high quality solution in an efficient manner.

5.4 Conclusion

The proposed approaches employ AI and ML algorithms to establish reliable connectivity. Considering important challenges inherent in dynamic planning problems, we devised to deliver a predictive outcome using a design time approach in which the solution is engineered to understand the dimensions of the problem and estimate the quality of the solution using experimental frame/GUI developed using react (Java script) and RapidMiner studio for interactive exploration of predictive models. The proposed predictive GUI framework will allow us to map out many options such as risks, objectives, profits and finally evaluate which course of action has the best chance of success while avoiding unnecessary risks or undesired outcomes.

Moreover, ongoing work is exploring promising research directions like online optimizations that have the potential to adaptively solve the recurring UE-AP association problem in an evolving network. The multiple best solutions that can be retrieved from such a changing network would make it possible to retrain and update the ML model that predicts the UE-AP association without the need for continuous optimization at deployment time. Hence, this contribution would further extend the hybrid AI/ML framework presented in chapter 4 of the deliverable D4.1.

Chapter 6

Optimal RIS Placement and Orientation

6.1 Introduction

The successful incorporation of RISs requires understanding of their performance under different RIS sizes, placements, and orientations. The RIS size relative to the footprint of the incident beam affects the received power, the RIS placement can reduce the blindspots of the RIS (e.g. with the walls restricting the motion of the user), while the RIS orientation can reduce the blindspots of the RIS or increase the in one direction to favour an area of interest.

There are several works that cover the assessment of optimal RIS placement in relation to the position of the access point (AP) and the user equipment (UE) [63–69]. The authors in [63] find the optimal placement of the RIS with respect to the signal-to-noise-ratio (SNR) at the receiver. When the footprint of the incident beam on the RIS is much larger than the RIS area, the optimal RIS placement is found to be near the UE, near the AP, or between the AP and the UE. When the footprint is smaller than the RIS, the optimal placement of the RIS is near the UE. In [64] the optimal placement of the RIS is studied in line-of-site (LoS) and non-line-of-sight (nLoS) environments for both single-input-single-output (SISO) and multiple-input-multiple-output (MIMO) systems. The authors find that with SISO systems the optimal RIS position is near the transmitter or the received. With MIMO systems, the optimal RIS position depends on the environment (LoS or nLoS). In LoS environments, the RIS can be placed close to or far from the transmitter and the receiver, while yielding a substantial gain in rate. On the other hand, in nLoS environments, the optimal RIS placement is close to the transmitter or the receiver. In [65], the author presents a strategy for the RIS deployment with the prospect of minimizing the blockage probability in the base station (BS)-RIS and RIS-UE links. In [66], the authors explore the difference between the centralized deployment with one RIS near the AP and the distributed deployment with two RIS near two users, each with half the number of elements of the centralized deployment.

However, the RIS orientation has so far not been studied thoroughly. In [67] the cell coverage is maximized by optimizing the RIS position and orientation. The authors deduce that the RIS normal pointing towards the BS is the optimal RIS orientation, but their analysis assumes full RIS illumination and fails to provide insight on their choices regarding the receiver. In [68, 69] the RIS placement and orientation are jointly studied

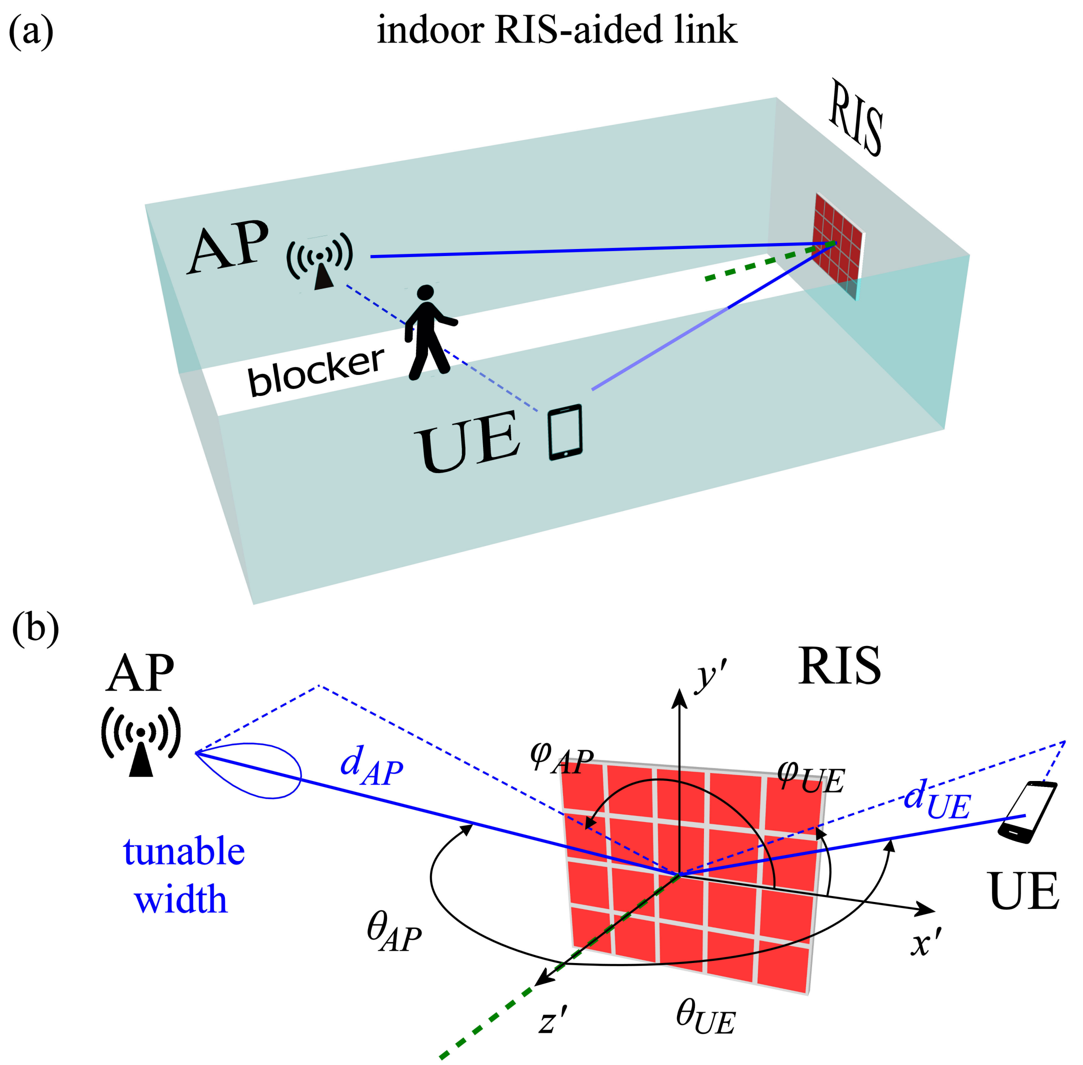

Figure 6.1: System model.

with the prospect of maximizing the received power in an indoors mobile user environment. Furthermore, in most of the previous works, the RIS is larger than the incident beam footprint and therefore it is fully illuminated. As THz frequencies are expected to be supported by pencil beams, it is necessary to understand the RIS efficiency under both full and partial illumination.

6.2 System Model

To study the effect of the RIS size relative to the size of the incident beam footprint and the RIS orientation on the RIS efficiency, the system model presented in Fig. (1) is considered. The centre of the RIS is considered to be at the origin of the local coordinate system and the RIS size is M×N elements. The AP-RIS distance is d_{AP} as shown in Fig. 6.1(b) with azimuth and elevation angles, relative to the RIS, ϕ_{AP} and θ_{AP} respectively. Similarly, the UE is at distance d_{UE} from the RIS. The RIS elements are positioned with periodicity d_x and d_y along the x and y-axis respectively. The AP is equipped with a direction antenna of tuneable gain, and it transmits towards the centre of the RIS, which redirects the towards the position of the UE. Both the AP-RIS and the RIS-UE links are without misalignment. The received power at the UE can be calculated as

$$P_r = S_r A_r \equiv \frac{|E_r|^2}{2Z_o} A_r, \tag{6.1}$$

where S_r and $A_r = (G_r \lambda^2)/4\pi$ and E_r are the power density, effective aperture and electric field at the position of the UE. The characteristic impedance of the air is Z_o, G_r is the antenna gain of the UE and λ is the wavelength. The total electric field at the UE is given by

$$E_r = \sum_{m=1}^{M} \sum_{n=1}^{N} E_{m,n}, \tag{6.2}$$

where the contribution of each (m,n) RIS element to the total electric field is [70, 71]

$$\begin{aligned} E_{m,n} = {} & \sqrt{2Z_o P_t G_t A_{RIS} G_{RIS}} \frac{\sqrt{U^t U^{RIS,t} U^{RIS,r} U^r}}{4\pi l^t_{m,n} l^r_{m,n}} \\ & |R_{m,n}| \exp\left(-j\phi_{m,n}\right) \exp\left(-j\frac{2\pi}{\lambda}(l^t_{m,n} + l^r_{m,n})\right). \end{aligned} \tag{6.3}$$

The transmitted power and the antenna gain of the AP are P_t and G_t, respectively and the effective aperture and gain of the RIS elements are A_{RIS} and G_{RIS}. Furthermore, the $l^t_{m,n}$ and $l^r_{m,n}$ are the distances between the (m,n) element and the AP, UE respectively, while $R_{m,n} = |R_{m,n}|$ is the complex reflection coefficient introduced by the (m,n) RIS element. The normalized radiation pattern of the AP, UE and the (m,n) RIS element are U^t, U^r and $U^{RIS,t/r}$, where the superscript t/r denotes the direction of the AP and the UE relative the RIS elements. In order to steer the reflected beam towards the UE, the linear phase gradient that the RIS imposes on the incident wave is given by [70, 71]

$$\begin{aligned} \phi_{m,n} = {} & \frac{2\pi}{\lambda}[(\sin\theta_{UE}\cos\phi_{UE} + \sin\theta_{AP}\cos\phi_{AP})x_m \\ & + (\sin\theta_{UE}\sin\phi_{UE} + \sin\theta_{AP}\sin\phi_{AP})y_n], \end{aligned} \tag{6.4}$$

where $x_m = m * d_x$ and $y_n = n * d_y$ are the coordinates of the (m,n) RIS element, with $m = 1, \ldots, M$ and $n = 1, \ldots, N$. The main lobe of the transmitted beam can be modelled as a Gaussian beam [72]. For normal incidence, the footprint of the incident beam on the RIS is circular, however under oblique incidence the footprint becomes elliptical with the ellipticity depending on both the angle θ_{AP} and distance d_{AP}. The power density of the incident beam footprint on the RIS can be expressed as [73]

$$S_{RIS} = \frac{2P_t}{\pi \frac{w^2_{RIS}}{\cos(\theta_{AP})}} e^{-2\frac{x^2}{\frac{w^2_{RIS}}{\cos(\theta_{AP})^2}}} e^{-2\frac{y^2}{w^2_{RIS}}}, \tag{6.5}$$

where w_{RIS} is the radius of the incident beam footprint at normal incidence and x and y are confined on the local coordinate system. The above equation accounts for oblique incidence on the horizontal, $x - z$, plane and results in the footprint being elongated along the $x-$axis. For normal incidence and partial RIS illumination, the power density at the UE can be estimated simply as [74]

$$S_r = \frac{\frac{2P_t}{\lambda z_R}|R|^2}{\sqrt{\left(1+\frac{d_{UE}^2}{z_R^2}\right)\left(1+\frac{d_{UE}^2}{z_R^2\cos^4\theta_{UE}}\right)}}. \tag{6.6}$$

where

$$z_R = \frac{kw_{RIS}^2}{2} = \frac{4kd_{AP}^2}{G_t}. \tag{6.7}$$

is the Rayleigh length and d_{UE} the RIS-UE distance.

6.3 Impact of the Steering Angle on Received Power

The RIS is considered lossless, and the total power of the reflected beam remains the same regardless of the steering direction of the UE. However, the beam begins to spread as it propagates towards the position of the UE, with the spreading becoming more notable with the increase of the steering angle, θ_{UE}. Consequently, the local power density of the reflected beam, and therefore the received power, depends considerably on the steering angle as shown in Fig.6.2. In the left panels, the RIS is fully illuminated and in the right panels it is partially illuminated. The top panels show the received power for all possible positions of the UE and the bottom panels show the received power of the three steering angles depicted with the coloured solid lines in the top panels, namely $\theta_{UE} = 0^o, 20^o$ and 40^o, along the grey dashed lines in the top panels. In the fully illuminated RIS case, due to the finite RIS size, sidelobes are generated besides the main lobe, while in the partially illuminated RIS case, where the RIS is much larger than the footprint of the incident beam, the reflected beam propagates as a single lobe. In both the full and partial illumination cases the reflected beam spreads as θ_{UE} increases. As a result, because the total beam power is conserved, the peak power decreases and, consequently, the power received by the UE decreases accordingly.

6.4 Optimal RIS Placement and Orientation

The position of the RIS in conjunction with its orientation can significantly affect the received power as shown in Fig. 6.3, where the received power at all possible positions of the UE is presented for two different RIS placements and orientations. In (a), the RIS is placed at the center of the right wall with the RIS normal pointing towards the center of the left wall and in (b), the RIS is placed at the top right corner with the RIS normal pointing towards the bottom left corner of the room. The transmitted power is 30 dBm, the radius of the circular incident beam footprint on the RIS is 5 cm and the antenna gain of the UE is 20 dB. The green dashed line shows the orientation of the RIS. As shown in Eq. 6.6, the power received by the UE decreases with the increase of d_{UE}

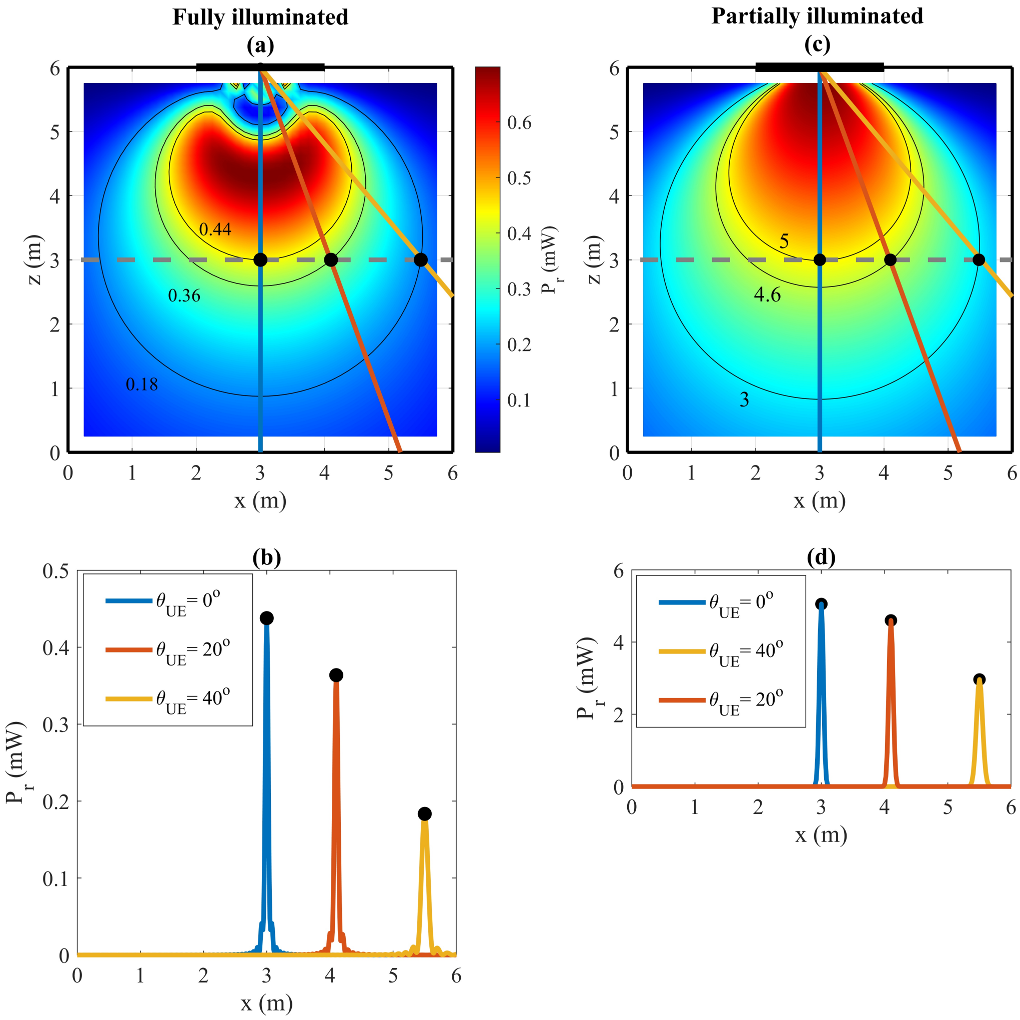

Figure 6.2: Spatial distribution of received power.

and θ_{UE}. Hence, the position and orientation of the RIS must minimize the maximum of both their values for all possible positions of the UE in the area of interest, in order to maximize the received power. It is observed that in (a), the minimum received power is determined by the region where $\theta_{UE} = 90^o$ and the received power there is reduced considerably. As a result, the minimum received power in (a) is -4.8 dBm. On the other hand, in (b) the position and orientation of the RIS eliminate this region as the maximum θ_{UE} is 51^o. The minimum received power in (b) is 3.8 dBm. However, in the area of interest marked with the blue rectangles, the situation is reversed. The RIS position and orientation in (a) favours the area of interest, as the minimum received power there is 5 dBm, while in (b) it is 4.2 dBm. The reason for this is that in (a) the maximum values of d_{UE} and θ_{UE} in the area of interest are lower than their values in (b). As a consequence, the optimal position and orientation are determined by the area of interest.

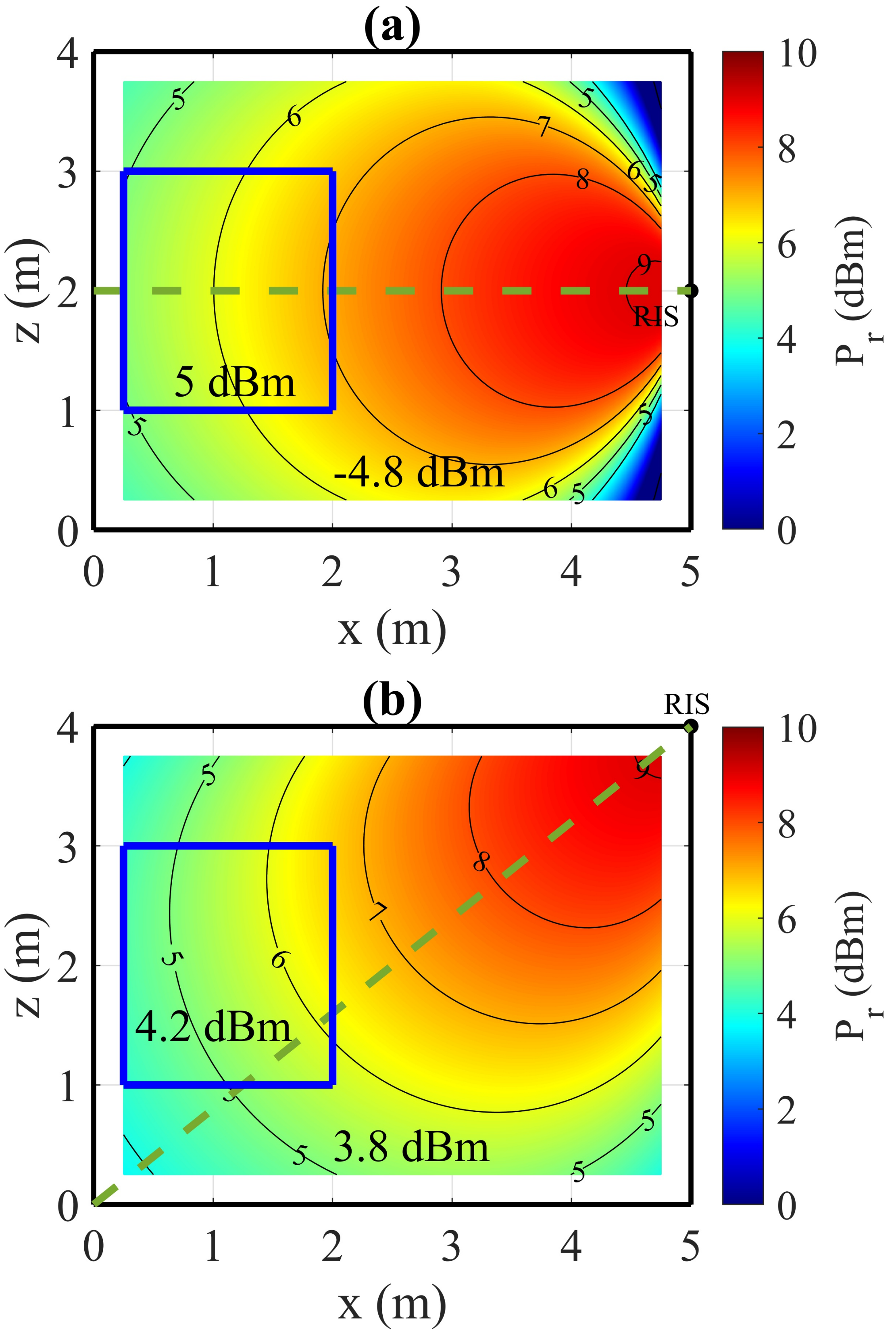

Figure 6.3: Received power in a 4×5 m^2 room with different RIS placements. In (a) the RIS is placed at the center of the right wall and is oriented towards the center of the left wall, while in (b) it is placed at the top right corner and is oriented towards the bottom left corner.

6.5 Full vs. Partial RIS Illumination Efficiency

With a fully illuminated RIS, only a part of the AP beam power is reflected, and the amount of power strongly depends on both the AP-RIS distance, d_{AP}, and the angle θ_{AP}. On the other hand, with a partially illuminated RIS all the power of the AP beam is reflected, and the position of the AP does not affect the total power that is reflected but the size of the incident beam footprint. In Fig. 6.4, the received power for all possible UE positions is presented with two different AP placements that are equidistant from the RIS and marked with a blue cross, and for both illumination conditions. The room size is 10×4 m^2 and the RIS is placed at $[4, 0, 10]$, which is the top right corner of the room, depicted with a black dot. The middle panels show the illumination conditions of the RIS. The top panel depicts the full illumination condition in (a) and (b) and the bottom panel the partial illumination condition in (c) and (d). For the partial RIS illumination case, the RIS size is 1000×250 RIS elements, which is large enough to capture the entire elliptical footprint and for the full illumination case, the RIS size is 250×250 elements. In (a) and (c) the AP, namely AP 1, is placed at $[0, 0, 5]$, which is the centre of the left wall and in (b) and (d) the AP, AP 2, is placed at $[4, 0, 3.6]$, which is on the right wall with equal distance from the RIS as AP 1. The distance, d_{AP}, is equal to 6.4 m, the direction of the AP in relation to the RIS is depicted with a blue dashed line and the RIS orientation, depicted with the green dashed line, is towards AP 1. This means that for AP 1 in (a) and (c), $\theta_o = 0^o$ and for AP 2 it is equal to 38.6^o. As d_{AP} is fixed for both positions of the AP, in (a) and (c) the received power is affected only by θ_{AP}. More specifically, the received power is proportional to $cos(\theta_{AP})$ (Eq. 6.5) as for relatively low AP gain, $S_{RIS} \rightarrow \frac{2}{\pi w_{RIS}} cos(\theta_{AP})$. This is the result of the full RIS illumination and the difference in received power between (a) and (c) can be simply estimated as $10log10\left(\frac{cos(\theta_{AP1})}{cos(\theta_{AP2})}\right)$. In (a) and (c), the difference is 1 dB. Though with full illumination the incident beam footprint is fixed and depends only on the dimensions of the RIS, with partial illumination the footprint can change depending on the position of the AP. This leads to a footprint-dependent performance. As an example, in Fig. 3 (c) the incident beam footprint is circular as $\theta_{AP} = 0^o$, but in (d) it is elliptical as $\theta_{AP} = 38.6^o$. As a result, the received power in (d) is higher than in (c).

As the RIS orientation and illumination condition affect the received power, the room coverage that is provided by the RIS (or RIS efficiency) is also affected. Room coverage expresses the percentage of the area of the room with received power at least equal to a threshold. The RIS efficiency as a metric, helps identify the optimal RIS position and orientation by showing which position and orientation achieves a certain power threshold in the entire room. As an example Fig. 6.5 shows the RIS orientation efficiency for the same room and topologies as in Fig. 6.4. In Fig. 6.5(a), the RIS is fully illuminated as the antenna gain of the AP is 35 dB and in Fig. 6.5(b) the RIS is partially illuminated as the AP antenna gain is 55 dB. The orientation angle, θ_o, is the angle between the top wall and the RIS normal as shown in (c). The power thresholds in (a) are $P_{th} = -15, -12, -10$ and -8 dBm, whle in (b) $P_{th} = -5, -2.5, 0$ and 2.5 dBm. Furthermore, although the AP-RIS distance is the same for both AP 1 and AP 2, their θ_{AP} changes with θ_o. For AP 1, $\theta_o = 0^o$ means $\theta_{AP} = 51^o$, while for AP 2 $\theta_{AP} = 90^o$. With full RIS illumination, the received power differs for AP 1 and AP 2 as shown in Fig. 6.4. Thus, the RIS orientation efficiency is also different between the two AP placements. In Fig. 6.5(a), the RIS orientation efficiency of AP 2 is observed to be lower than the

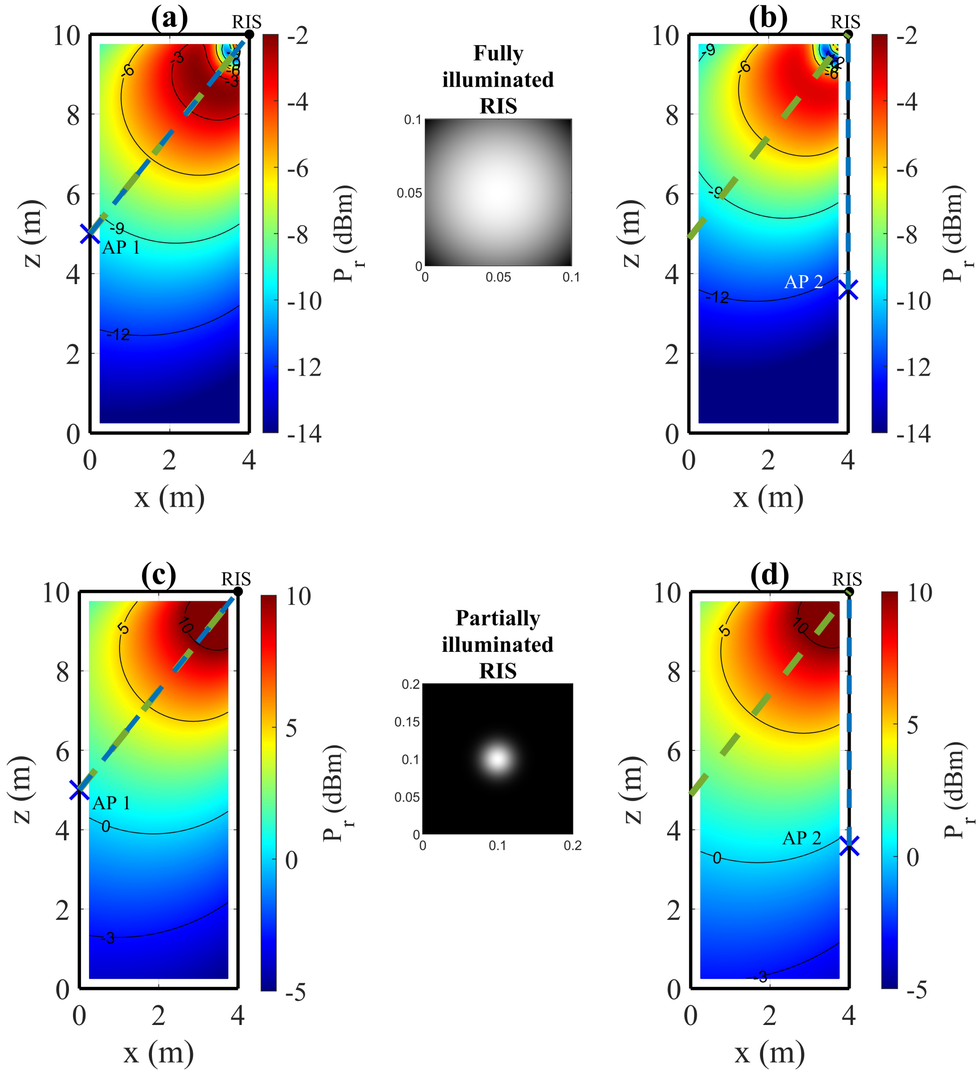

Figure 6.4: Received power in a 10×4 m^2 room with different, but equidistant from the RIS, AP placements, for both partial and full illumination cases.

efficiency of AP 1 for the majority of θ_o values. This is the result of the θ_{AP} of AP 2 being higher than the θ_{AP} of AP 1. When $\theta_o = 70^o$ the RIS normal points towards the opposite corner of the room ($[0, 0, 0]$). With this orientation the efficiency of both AP placements is the same as θ_{AP} is the same for both of them. For $\theta_o > 70^o$ the efficiency of AP 2 is higher than the efficiency of AP 1 as θ_{AP} is lower for AP 2 than for AP 1. In the case of partial illumination shown in Fig. 6.5(b), the footprint of the incident beam is elongated as θ_{AP} increases and therefore the results are observed to be opposite to the full illumination case. The efficiency of AP 2 is higher than the efficiency of AP 1 for most values of θ_o.

6.6 Conclusion

In this chapter, the position and orientation of the RIS was studied in terms of received power and efficiency. In order to understand how the received power depends on the position, orientation and size of the RIS, simulations were performed for both

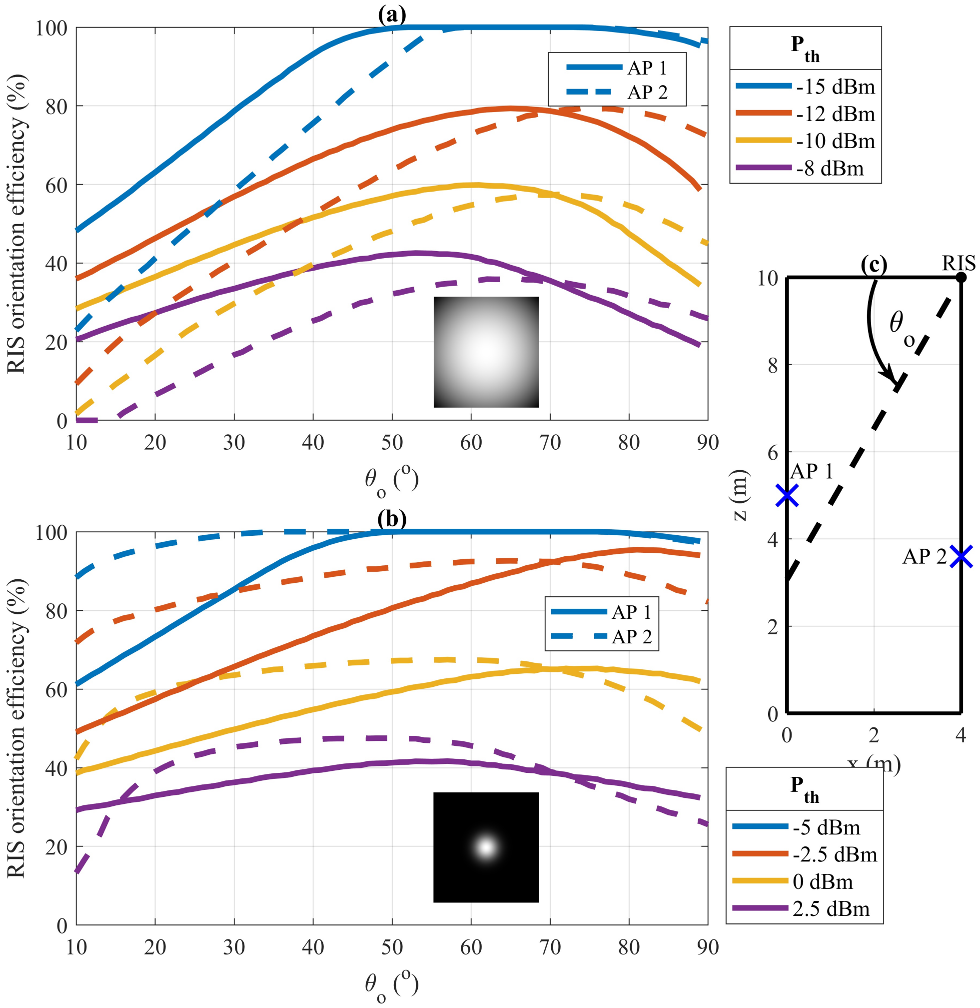

Figure 6.5: RIS orientation efficiency vs orientation angle θ_o.

fully and partially illuminated RISs, with different positions and orientations. It was shown that the minimum received power in an area of interest is significantly dependent on the position and orientation of the RIS. Furthermore, the RIS efficiency depends on the RIS orientation in relation to the position of the UE as the orientation directly affects the angle θ_{UE}. In the simulations, a D-band indoor scenario was assumed, but the findings can be extended to an outdoor with different frequency band.

Conclusions

In conclusion, the results reported in deliverable D4.3 clearly substantiate the potential gains of using RISs for making data transmission and communication in high frequency wireless networks both reliable and efficient with the aid of machine learning. In particular, the main obtained results and findings can be summarized as follows.

In **chapter 1**, a deep unfolding model for efficiently estimating the end-to-end RIS channel in SIMO systems has been introduced. The proposed approach outperformed three benchmark schemes based on the LS method, a CVX-based numerical solution of the channel estimation problem, and the ANM algorithm, taking into account: the impact of the number of paths, the training SNR, and the angular parameter distribution on the estimation accuracy.

In **chapter 2**, an RIS power consumption model capturing the RIS main power-consuming electronic components was proposed. The autonomous operation was guaranteed by a provided range of average power consumption of the RIS electronics.

In **chapter 3**, four typical scenarios of RIS-aided multi-user communications have been presented. As performance evaluations revealed, distributed AI-assisted MAC schemes are more applicable to networks with small numbers of users associated with a large number of RISs. In contrast, the centralized AI-assisted MAC schemes are more suitable for a large number of users in conjunction with small numbers of RISs.

In **chapter 4**, the ARIADNE updated system level simulation model for D-band networks focusing on user's mobility model and path loss modelling was presented.

In **chapter 5**, ML algorithms to establish reliable connectivity were presented. Considering important challenges inherent in dynamic planning, we devised to deliver a predictive outcome using a design time approach in which the solution is engineered to understand the dimensions of the problem and estimate the quality of the solution using experimental frame/GUI developed using react (Java script) and RapidMiner studio for interactive exploration of predictive models.

In **chapter 6**, the position and orientation of an RIS was studied in terms of received power and efficiency. Results show that the minimum received power in an area of interest depends on the position and orientation of the RIS. Furthermore, the RIS efficiency depends on the RIS orientation in relation to the position of a UE.

Deliverable D4.3 constitutes a major advance of WP4 within the ARIADNE project. Overall, the results reported in this deliverable allowed us to assess the major performance gains that the deployment of AI-enhanced RISs in high frequency bands bring about for application to future wireless communication systems.

Bibliography

[1] Q. Wu and R. Zhang, "Intelligent reflecting surface enhanced wireless network via joint active and passive beamforming," *IEEE Trans. Wireless Commun.*, vol. 18, pp. 5394–5409, Nov. 2019.

[2] C. Liaskos, A. Tsioliaridou, A. Pitsillides, S. Ioannidis, and I. F. Akyildiz, "Using any surface to realize a new paradigm for wireless communications," *Communications of the ACM*, vol. 61, pp. 30–33, 2018.

[3] M. Di Renzo *et al.*, "Smart radio environments empowered by reconfigurable AI meta-surfaces: an idea whose time has come," *EURASIP J. Wireless Comm. and Networking*, vol. 2019, p. 129, 2019.

[4] H. Wymeersch, J. He, B. Denis, A. Clemente, and M. Juntti, "Radio localization and mapping with reconfigurable intelligent surfaces: Challenges, opportunities, and research directions," vol. 15, no. 4, pp. 52–61, 2020.

[5] D. Li, "Fairness-aware multiuser scheduling for finite-resolution intelligent reflecting surface-assisted communication," vol. 25, no. 7, pp. 2395–2399, 2021.

[6] M. Di Renzo *et al.*, "Smart radio environments empowered by reconfigurable intelligent surfaces: How it works, state of research, and the road ahead," vol. 38, no. 11, pp. 2450–2525, 2020.

[7] E. Basar *et al.*, "Wireless communications through reconfigurable intelligent surfaces," *IEEE Access*, vol. 7, pp. 116753–116773, 2019.

[8] J. He, M. Leinonen, H. Wymeersch, and M. Juntti, "Channel estimation for RIS-aided mmWave MIMO channels," in *proc. IEEE Global Communications Conference*, pp. 1–6, 2020.

[9] J. He, H. Wymeersch, and M. Juntti, "Channel estimation for RIS-aided mmWave MIMO systems via atomic norm minimization," pp. 1–1, 2021.

[10] Z. He and X. Yuan, "Cascaded channel estimation for large intelligent metasurface assisted massive MIMO," vol. 9, pp. 210–214, Feb 2020.

[11] A. Zappone, M. Di Renzo, and M. Debbah, "Wireless networks design in the era of deep learning: Model-based, AI-based, or both?," vol. 67, no. 10, pp. 7331–7376, 2019.

[12] K. Tekbıyık, G. K. Kurt, C. Huang, A. R. Ekti, and H. Yanikomeroglu, "Channel estimation for full-duplex RIS-assisted HAPS backhauling with graph attention networks," in *proc. IEEE ICC*, pp. 1–6, 2021.

[13] A. M. Elbir, A. Papazafeiropoulos, P. Kourtessis, and S. Chatzinotas, "Deep channel learning for large intelligent surfaces aided mm-wave massive MIMO systems," vol. 9, no. 9, pp. 1447–1451, 2020.

[14] N. Samuel, T. Diskin, and A. Wiesel, "Learning to detect," vol. 67, no. 10, pp. 2554–2564, 2019.

[15] K. Gregor and Y. LeCun, "Learning fast approximations of sparse coding," in *proc. international conference on machine learning*, pp. 399–406, 2010.

[16] J. He, H. Wymeersch, M. Di Renzo, and M. Juntti, "Learning to estimate ris-aided mmwave channels," pp. 1–1, 2022.

[17] N. Landsberg and E. Socher, "A low-power 28-nm CMOS FD-SOI reflection amplifier for an active F-band reflectarray," *IEEE Transactions on Microwave Theory and Techniques*, vol. 65, no. 10, pp. 3910–3921, 2017.

[18] Y. Chen and Y. Chi, "Harnessing structures in big data via guaranteed low-rank matrix estimation: Recent theory and fast algorithms via convex and nonconvex optimization," vol. 35, no. 4, pp. 14–31, 2018.

[19] J. G. Andrews *et al.*, "What Will 5G Be?," *IEEE Journal on Selected Areas in Communications*, vol. 32, no. 6, pp. 1065–1082, 2014.

[20] W. Khawaja, O. Ozdemir, Y. Yapici, F. Erden, and I. Guvenc, "Coverage Enhancement for NLOS mmwave Links Using Passive Reflectors," *IEEE Open Journal of the Communications Society*, vol. 1, pp. 263–281, 2020.

[21] M. Di Renzo *et al.*, "Smart Radio Environments Empowered by Reconfigurable Intelligent Surfaces: How It Works, State of Research, and The Road Ahead," *IEEE Journal on Selected Areas in Communications*, vol. 38, no. 11, pp. 2450–2525, 2020.

[22] E. Björnson, Ö. Özdogan, and E. G. Larsson, "Reconfigurable intelligent surfaces: Three myths and two critical questions," *IEEE Commun. Mag.*, no. 12, pp. 90–96, 2020.

[23] S. Kisseleff, W. A. Martins, H. Al-Hraishawi, S. Chatzinotas, and B. Ottersten, "Reconfigurable Intelligent Surfaces for Smart Cities: Research Challenges and Opportunities," *IEEE Open Journal of the Communications Society*, vol. 1, 2020.

[24] A.-A. A. Boulogeorgos and A. Alexiou, "Performance Analysis of Reconfigurable Intelligent Surface-Assisted Wireless Systems and Comparison With Relaying," *IEEE Access*, vol. 8, pp. 94463–94483, May 2020.

[25] M. D. Renzo *et al.*, "Reconfigurable intelligent surfaces vs. relaying: Differences, similarities, and performance comparison," *IEEE Open Journal of the Communications Society*, vol. 1, pp. 798–807, June 2020.

[26] E. Björnson, O. Özdogan, and E. G. Larsson, "Intelligent Reflecting Surface vs. Decode-and-Forward: How Large Surfaces Are Needed to Beat Relaying?," *IEEE Wirel. Commun. Lett.*, vol. 9, no. 2, pp. 244–248, 2020.

[27] C. Pan *et al.*, "Intelligent Reflecting Surface Aided Mimo Broadcasting for Simultaneous Wireless Information and Power Transfer," *IEEE J. Sel. Areas Commun.*, vol. 38, no. 8, pp. 1719–1734, 2020.

[28] Q. Wu and R. Zhang, "Joint Active and Passive Beamforming Optimization for Intelligent Reflecting Surface Assisted SWIPT Under QoS Constraints," *IEEE J. Sel. Areas Commun.*, vol. 38, no. 8, pp. 1735–1748, 2020.

[29] Y. Zou, S. Gong, J. Xu, W. Cheng, D. T. Hoang, and D. Niyato, "Wireless Powered Intelligent Reflecting Surfaces for Enhancing Wireless Communications," *IEEE Transactions on Vehicular Technology*, vol. 69, no. 10, pp. 12369–12373, 2020.

[30] Hu, Shaokang and Wei, Zhiqiang and Cai, Yuanxin and Liu, Chang and Ng, Derrick Wing Kwan and Yuan, Jinhong, "Robust and Secure Sum-Rate Maximization for Multiuser MISO Downlink Systems With Self-Sustainable IRS," *IEEE Transactions on Communications*, vol. 69, no. 10, 2021.

[31] K. Ntontin, A.-A. A. Boulogeorgos, D. G. Selimis, F. I. Lazarakis, A. Alexiou, and S. Chatzinotas, "Reconfigurable Intelligent Surface Optimal Placement in Millimeter-Wave Networks," *IEEE Open Journal of the Communications Society*, vol. 2, pp. 704–718, 2021.

[32] D. Schulz *et al.*, "Robust optical wireless link for the backhaul and fronthaul of small radio cells," *Journal of Lightwave Technology*, vol. 34, no. 6, pp. 1523–1532, 2016.

[33] M. Al-Jarrah, E. Alsusa, A. Al-Dweik, and M.-S. Alouini, "Performance Analysis of Wireless Mesh Backhauling Using Intelligent Reflecting Surfaces," *IEEE Trans. Wirel. Commun.*, to appear.

[34] I. A. Hemadeh, K. Satyanarayana, M. El-Hajjar, and L. Hanzo, "Millimeter-Wave Communications: Physical Channel Models, Design Considerations, Antenna Constructions, and Link-Budget," *IEEE Communications Surveys Tutorials*, vol. 20, no. 2, pp. 870–913, 2018.

[35] A. Chakraborty and B. Gupta, "Paradigm Phase Shift: Rf Mems Phase Shifters: An Overview," *IEEE Microwave Magazine*, vol. 18, no. 1, pp. 22–41, 2017.

[36] A. A. G. Amer, S. Z. Sapuan, N. Nasimuddin, A. Alphones, and N. B. Zinal, “A comprehensive review of metasurface structures suitable for rf energy harvesting,” *IEEE Access*, vol. 8, pp. 76433–76452, 2020.

[37] S. Abadal, T. Cui, T. Low, and J. Georgiou, “Programmable metamaterials for software-defined electromagnetic control: Circuits, systems, and architectures,” *IEEE Journal on Emerging and Selected Topics in Circuits and Systems*, vol. 10, no. 1, pp. 6–19, 2020.

[38] A. C. Tasolamprou *et al.*, “Exploration of intercell wireless millimeter-wave communication in the landscape of intelligent metasurfaces,” *IEEE Access*, vol. 7, pp. 122931–122948, 2019.

[39] L. Petrou, P. Karousios, and J. Georgiou, “Asynchronous Circuits as an Enabler of Scalable and Programmable Metasurfaces,” in *2018 IEEE International Symposium on Circuits and Systems (ISCAS)*, 2018.

[40] S. Abeywickrama, R. Zhang, Q. Wu, and C. Yuen, “Intelligent Reflecting Surface: Practical Phase Shift Model and Beamforming Optimization,” *IEEE Tran. Commun.*, vol. 68, no. 9, pp. 5849–5863, 2020.

[41] J. Zhang, X. Wei, I. D. Rukhlenko, H.-T. Chen, and W. Zhu, “Electrically Tunable Metasurface with Independent Frequency and Amplitude Modulations,” *ACS Photonics*, vol. 7, pp. 265–271, Dec. 2019.

[42] T. Saeed *et al.*, “Workload Characterization of Programmable Metasurfaces,” in *ACM NANOCOM 2019*, Sep. 2019.

[43] M. Di Renzo, M. Debbah, D. Phan-Huy, A. Zappone, M. Alouini, C. Yuen, V. Sciancalepore, G. C. Alexandropoulos, J. Hoydis, and j. . E. y. . . v. . . n. . . p. . . H. Gacanin *et al.*, title = Smart Radio Environments Empowered by Reconfigurable AI Meta-Surfaces: An Idea Whose Time Has Come

[44] S. Gong, X. Lu, D. T. Hoang, D. Niyato, L. Shu, D. I. Kim, , and Y. Liang, “Towards smart wireless communications via intelligent reflecting surfaces: A contemporary survey,” *IEEE Communications Surveys & Tutorials*, vol. 22, no. 4, pp. 2283–2314, 2020.

[45] Y. Yang, B. Zheng, S. Zhang, and R. Zhang, “Intelligent reflecting surface meets ofdm: Protocol design and rate maximization,” *IEEE Transactions on Communications*, vol. 68, no. 7, pp. 4522–4535, 2020.

[46] S. Lin, B. Zheng, G. C. Alexandropoulos, M. Wen, F. Chen, and S. Mumtaz, “Adaptive transmission for reconfigurable intelligent surface-assisted ofdm wireless communications,” *IEEE Journal on Selected Areas in Communications*, vol. 38, no. 11, pp. 2653–2665, 2020.

[47] C. You, B. Zheng, and R. Zhang, “Channel estimation and passive beamforming for intelligent reflecting surface: Discrete phase shift and progressive refinement,” *IEEE Journal on Selected Areas in Communications*, vol. 38, no. 11, pp. 2604–2620, 2020.

[48] J. Hu, H. Zhang, B. Di, L. Li, K. Bian, L. Song, Y. Li, Z. Han, and H. V. Poor, “Reconfigurable intelligent surface based rf sensing: Design, optimization, and implementation,” *IEEE Journal on Selected Areas in Communications*, vol. 38, no. 11, pp. 2700–2716, 2020.

[49] S. Li, B. Duo, X. Yuan, Y. Liang, and M. D. Renzo, “Reconfigurable intelligent surface assisted uav communication: Joint trajectory design and passive beamforming,” *IEEE Wireless Communications Letters*, vol. 9, no. 5, pp. 716–720, 2020.

[50] T. Bai, C. Pan, Y. Deng, M. Elkashlan, A. Nallanathan, and L. Hanzo, “Latency minimization for intelligent reflecting surface aided mobile edge computing,” *IEEE Journal on Selected Areas in Communications*, vol. 38, no. 11, pp. 2666–2682, 2020.

[51] M. Jung, W. Saad, M. Debbah, and C. S. Hong, “On the optimality of reconfigurable intelligent surfaces (riss): Passive beamforming, modulation, and resource allocation,” *IEEE Transactions on Wireless Communications*, 2021.

[52] H. Guo, Y. Liang, J. Chen, and E. G. Larsson, “Weighted sum-rate maximization for reconfigurable intelligent surface aided wireless networks,” *IEEE Transactions on Wireless Communications*, vol. 19, no. 5, pp. 3064–3076, 2020.

[53] Z. Ding and H. V. Poor, “A simple design of irs-noma transmission,” *IEEE Communications Letters*, vol. 24, no. 5, pp. 1119–1123, 2020.

[54] G. Yang, X. Xu, and Y. Liang, “Intelligent reflecting surface assisted non-orthogonal multiple access,” in *in* IEEE Wireless Communications and Networking Conference (WCNC), 2020.

[55] X. Cao, B. Yang, H. Zhang, C. Huang, C. Yuen, and Z. Han, “Reconfigurable intelligent surface-assisted mac for wireless networks: Protocol design, analysis, and optimization,” *IEEE Internet of Things Journal*, 2021.

[56] C. Papageorgiou, K. Birkos, T. Dagiuklas, and S. Kotsopoulos, “An obstacle-aware human mobility model for ad hoc networks,” in *2009 IEEE International Symposium on Modeling, Analysis & Simulation of Computer and Telecommunication Systems*, pp. 1–9, IEEE, 2009.

[57] A. Goldsmith, *Wireless communications*. Cambridge university press, 2005.

[58] Y. Xing and T. S. Rappaport, “Propagation measurements and path loss models for sub-thz in urban microcells,” *arXiv preprint arXiv:2103.01151*, 2021.

[59] O. Dharmadhikari, “Leveraging machine learning and artificial intelligence for 5g,” tech. rep., CableLabs, 2019.

[60] A. Haidine, F. Z. Salmam, A. Aqqal, and A. Dahb, *Artificial Intelligence and Machine Learning in 5G and beyond: A Survey and Perspectives*. 2021.

[61] O. Zemer, “How machine learning will boost 5g network performance,” tech. rep., Forbes Technology council, 2020.

[62] “Cross-industry standard process for data mining.” `https://en.wikipedia.org/wiki/Cross-industry_standard_process_for_data_mining`.

[63] K. Ntontin, A.-A. A. Boulogeorgos, D. G. Selimis, F. I. Lazarakis, A. Alexiou, and S. Chatzinotas, “Reconfigurable intelligent surface optimal placement in millimeter-wave networks,” *IEEE Open Journal of the Communications Society*, vol. 2, pp. 704–718, 2021.

[64] E. Ibrahim, R. Nilsson, and J. van de Beek, “On the position of intelligent reflecting surfaces,” in *2021 Joint European Conference on Networks and Communications 6G Summit (EuCNC/6G Summit)*, pp. 66–71, 2021.

[65] G. Ghatak, “On the placement of intelligent surfaces for rssi-based ranging in mm-wave networks,” *IEEE Communications Letters*, vol. 25, no. 6, pp. 2043–2047, 2021.

[66] S. Zhang and R. Zhang, “Intelligent reflecting surface aided multi-user communication: Capacity region and deployment strategy,” *IEEE Transactions on Communications*, vol. 69, no. 9, pp. 5790–5806, 2021.

[67] S. Zeng, H. Zhang, B. Di, Z. Han, and L. Song, “Reconfigurable intelligent surface (RIS) assisted wireless coverage extension: RIS orientation and location optimization,” *IEEE Commun. Lett.*, pp. 1–1, Nov. 2020.

[68] G. Stratidakis, S. Droulias, and A. Alexiou, “An analytical framework for reconfigurable intelligent surfaces placement in a mobile user environment,” in *Proceedings of the 19th ACM Conference on Embedded Networked Sensor Systems*, SenSys ’21, (New York, NY, USA), p. 623–627, Association for Computing Machinery, 2021.

[69] G. Stratidakis, S. Droulias, and A. Alexiou, “Optimal position and orientation study of reconfigurable intelligent surfaces in a mobile user environment,” 2022 [Unpublished].

[70] W. Tang, M. Z. Chen, X. Chen, J. Y. Dai, Y. Han, M. D. Renzo, Y. Zeng, S. Jin, Q. Cheng, and T. J. Cui, “Wireless communications with reconfigurable intelligent surface: Path loss modeling and experimental measurement,” *IEEE Transactions on Wireless Communications*, vol. 20, pp. 421–439, Jan 2021.

[71] A.-A. A. Boulogeorgos and A. Alexiou, “Coverage analysis of reconfigurable intelligent surface assisted THz wireless systems,” *IEEE Open Journal of Vehicular Technology*, pp. 1–1, 2021.

[72] A. Kazemipour, M. Hudlička, R. Dickhoff, M. Salhi, T. Kleine-Ostmann, and T. Schrader, “The horn antenna as gaussian source in the mm-wave domain,” *Journal of Infrared, Millimeter, and Terahertz Waves*, vol. 35, pp. 720–731, Jun 2014.

[73] G. Stratidakis, S. Droulias, and A. Alexiou, “Understanding the ris efficiency: from partial to full illumination,” 2022 [Unpublished].

[74] G. Stratidakis, S. Droulias, and A. Alexiou, “Analytical performance assessment of beamforming efficiency in reconfigurable intelligent surface-aided links,” *IEEE Access*, vol. 9, pp. 115922–115931, 2021.